



AFRL-AFOSR-JP-TR-2016-0041

---

## Coupling Graphene Sheets with Iron Oxide Nanoparticles for Energy Storage and Microelectronics

Andre-Jean Attias  
UNIVERSITE PARIS 6 PIERRE ET MARIE CURIE

---

04/22/2016  
Final Report

DISTRIBUTION A: Distribution approved for public release.

Air Force Research Laboratory  
AF Office Of Scientific Research (AFOSR)/ IOA  
Arlington, Virginia 22203  
Air Force Materiel Command

Distribution A: Approved for public release; distribution is unlimited.

<b>REPORT DOCUMENTATION PAGE</b>					Form Approved OMB No. 0704-0188	
<p>The public reporting burden for this collection of information is estimated to average 1 hour per response, including the time for reviewing instructions, searching existing data sources, gathering and maintaining the data needed, and completing and reviewing the collection of information. Send comments regarding this burden estimate or any other aspect of this collection of information, including suggestions for reducing the burden, to Department of Defense, Executive Services, Directorate (0704-0188). Respondents should be aware that notwithstanding any other provision of law, no person shall be subject to any penalty for failing to comply with a collection of information if it does not display a currently valid OMB control number.</p> <p>PLEASE DO NOT RETURN YOUR FORM TO THE ABOVE ORGANIZATION.</p>						
<b>1. REPORT DATE (DD-MM-YYYY)</b> 22-04-2016		<b>2. REPORT TYPE</b> Final		<b>3. DATES COVERED (From - To)</b> 30 Mar 2012 to 20 May 2015		
<b>4. TITLE AND SUBTITLE</b> Coupling Graphene Sheets with Iron Oxide Nanoparticles for Energy Storage and Microelectronics				<b>5a. CONTRACT NUMBER</b> FA2386-12-1-4011		
				<b>5b. GRANT NUMBER</b> Grant 12RSZ071_124011		
				<b>5c. PROGRAM ELEMENT NUMBER</b> 61102F		
<b>6. AUTHOR(S)</b> Andre-Jean Attias				<b>5d. PROJECT NUMBER</b>		
				<b>5e. TASK NUMBER</b>		
				<b>5f. WORK UNIT NUMBER</b>		
<b>7. PERFORMING ORGANIZATION NAME(S) AND ADDRESS(ES)</b> UNIVERSITE PARIS 6 PIERRE ET MARIE CURIE 4 PLACE JUSSIEU PARIS, 75005 FR				<b>8. PERFORMING ORGANIZATION REPORT NUMBER</b>		
<b>9. SPONSORING/MONITORING AGENCY NAME(S) AND ADDRESS(ES)</b> AOARD UNIT 45002 APO AP 96338-5002				<b>10. SPONSOR/MONITOR'S ACRONYM(S)</b> AFRL/AFOSR/IOA(AOARD)		
				<b>11. SPONSOR/MONITOR'S REPORT NUMBER(S)</b> 12RSZ071_124011		
<b>12. DISTRIBUTION/AVAILABILITY STATEMENT</b> Distribution Code A: Approved for public release, distribution is unlimited.						
<b>13. SUPPLEMENTARY NOTES</b>						
<b>14. ABSTRACT</b> The principle of supramolecular chemistry has been implemented for the effort. The supramolecular chemistry offers promising routes to design specific molecular assemblies fulfilling the needs of functional surfaces by noncovalent functionalization to enhance magnetic properties of organic-inorganic nanomaterials. The effort of the project demonstrates the potential of supramolecular characteristics as result of 2D nanoporous organic matrix capable of capturing the inorganic magnetic nanocrystals.						
<b>15. SUBJECT TERMS</b> Electromagnetic Materials, Graphene, Nanocomposites, Nanoparticles						
<b>16. SECURITY CLASSIFICATION OF:</b>			<b>17. LIMITATION OF ABSTRACT</b>  SAR	<b>18. NUMBER OF PAGES</b>  35	<b>19a. NAME OF RESPONSIBLE PERSON</b> MAH, MISOOON	
<b>a. REPORT</b>  Unclassified	<b>b. ABSTRACT</b>  Unclassified	<b>c. THIS PAGE</b>  Unclassified			<b>19b. TELEPHONE NUMBER (Include area code)</b> 042-511-2001	

Standard Form 298 (Rev. 8/98)  
Prescribed by ANSI Std. Z39.18

Distribution A: Approved for public release; distribution is unlimited.

# **FINAL REPORT FOR AOARD PROJECT**

## **<France-Korea-USA Joint Project>**

**Title**  
**“Coupling Graphene Sheets with Magnetic Nanoparticles for  
Energy Storage and Microelectronics”**

**August 13, 2015**

### **Principle Investigators**

**Korean PI :** Kwang-Sup Lee, Department of Advanced Materials, Hannam University,  
Daejeon, S. Korea (E-mail: kslee@hnu.kr / kslee8857@gmail.com)

**USA PI :** Alex K-Y. Jen, Department of Materials Science & Engineering,  
University of Washington, Seattle, USA (E-mail: ajen@u.washington.edu)

**French PI :** André-Jean Attias, Univ. Pierre et Marie Curie (Paris 6 University), Paris,  
France (E-mail: andre-jean.attias@upmc.fr)

### **AOARD-AFOSR Program Manager:**

Dr. Misoon Mah  
Asian Office of Aerospace Research and Development (AOARD)  
7-23-17 Roppongi, Minato-Ku, Tokyo 106-0032, Japan

## CONTENTS

### **Prof. Kwang-Sup Lee (Korean PI)**

1. Abstract	3
2. Introduction	3
2.1. Background	3
2.2. Motivation	3
3. Results and Discussion	3
3.1. Pyrene-Dopamine (PyDop) Ligands	4
3.2. Synthesis of Superparamagnetic $\gamma$ -Fe <sub>2</sub> O <sub>3</sub> Nanoparticles	6
3.3. Coupling $\gamma$ -Fe <sub>2</sub> O <sub>3</sub> Nanoparticles with Ligands	6
3.4. Coupling PyDop- $\gamma$ -Fe <sub>2</sub> O <sub>3</sub> Nanoparticles with Graphene Derivatives	9
3.4.1. PyDop1- $\gamma$ -Fe <sub>2</sub> O <sub>3</sub> -GO/GNP Nanosheets	9
3.4.2. PyDop2- $\gamma$ -Fe <sub>2</sub> O <sub>3</sub> -GO/GNP Nanosheets	9
3.4.3. PyDop3- $\gamma$ -Fe <sub>2</sub> O <sub>3</sub> -GO/GNP Nanosheets	10
3.4.4. PyDop1- $\gamma$ -Fe <sub>2</sub> O <sub>3</sub> -Graphene Sheets	11
3.4.5. PyDop1- $\gamma$ -Fe <sub>2</sub> O <sub>3</sub> -Chemically Converted Graphene	12
3.5. Tunable Memories with PyDop1- $\gamma$ -Fe <sub>2</sub> O <sub>3</sub> -Graphene Oxide Charge Trapping Layer	13
4. Conclusions	15
5. References	15

### **Prof. Alex K. Jen (USA PI)**

1. Abstract	16
2. Introduction	16
2.1. Background	16
2.2. Motivation	17
3. Results and Discussion	18
4. Conclusions	25
5. References	25

### **Prof. Andre-Jean Attias (French PI)**

1. Introduction	27
2. Results and Discussion	27
2.1. Supramolecular Self-assembly on Graphene	27
2.2. Synthesis of Building Blocks bearing Ligands	29
2.3. Adsorption of Nanoparticles	31
3. Conclusions	31
4. References	31

<b><u>Publications and Presentations</u></b>	32
--	----

**“Non-Covalent Coupling of Superparamagnetic Nanoparticles to Graphene and Their Applications”**

**1. Abstract**

In this report we summarize our studies into a group of pyrene-spacer-dopamine (PyDop) ligands capable of noncovalently coupling superparamagnetic  $\gamma$ -Fe<sub>2</sub>O<sub>3</sub> magnetic nanoparticles (MNP) to graphene-based materials. The distance of the ligands to the graphene derivative surface can be varied by changing the spacer length. This project has been successful in the demonstration of high density coupling of PyDop functionalized MNPs onto different types of graphene materials like reduced graphene oxide (rGO) nanoplatelets, chemically reduced graphene as well as electrochemically exfoliated graphene. Some early results demonstrating the applicability of reduced graphene oxide-PyDop- $\gamma$ -Fe<sub>2</sub>O<sub>3</sub> as a charge trapping layer in memory transistors are also presented.

**2. Introduction**

**2.1. Background**

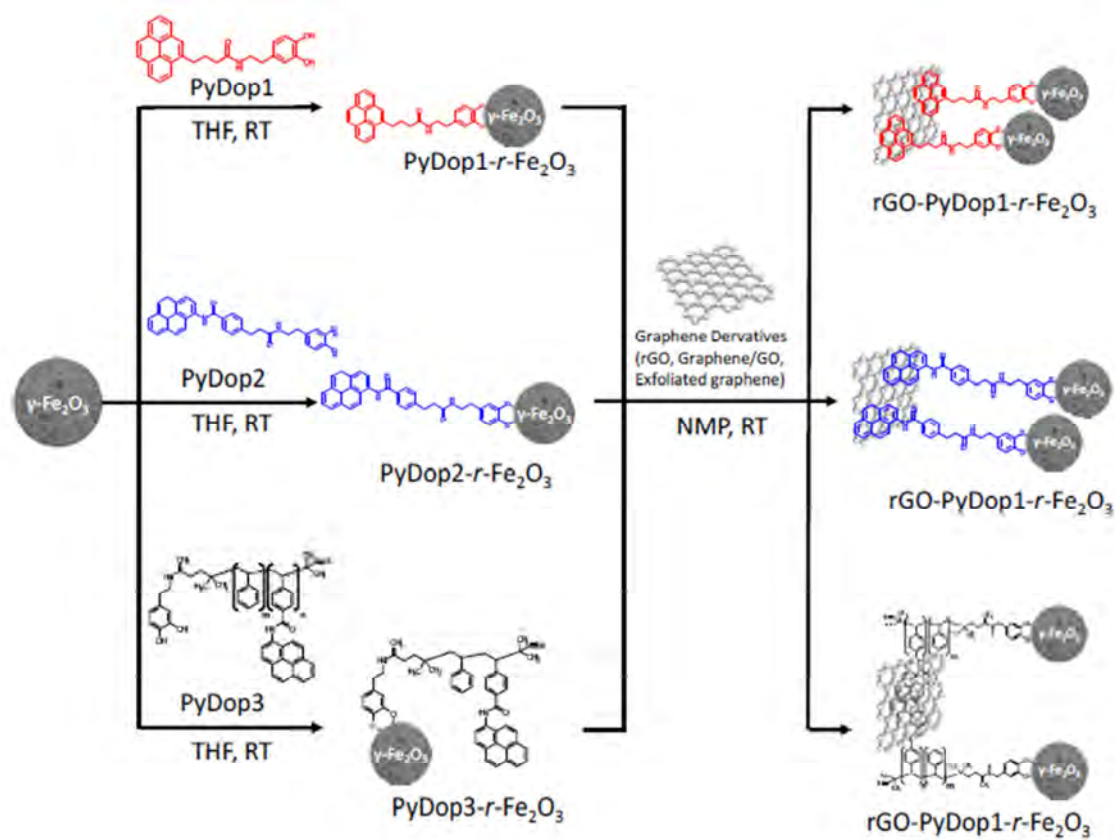
The discovery of graphene has led to a flurry of activity in the properties of two-dimensional materials [1-2]. During the past decade it has led to the discovery of a new generation of materials with remarkable physical, electronic and photonic properties. Invariably graphene has led the pack and every year this material is understood more, and applied more. It has opened up new challenges to the material scientist right from its large scale synthesis to the harnessing of its properties. Graphene in its pure form is notoriously insoluble and hence hard to combine to other materials to form functional nanocomposites. The cheapest method to make a graphenic material is by chemical exfoliation of graphite, but this process yields an oxidized version of graphene with properties that are a far cry from the legend of graphene [3]. There are other more expensive processes like chemical vapor deposition (CVD) to produce versions of graphene with superior properties [4]. The applicability of graphene depends largely on combining it with other nanomaterials. A lot of reported works deals with chemical modification of residual groups on the surface of graphene. This approach has a drawback that direct functionalization of graphene changes its remarkable electronic properties. An alternative approach is to use electron rich aromatic ligands that could non-covalently couple with graphene [5]. In this project we explore this approach by design, synthesis and study of ligands capable of non-covalently interacting with graphene while coupling it to nanoparticles. Such materials have predicted applications in energy storage and electronics.

**2.2. Motivation**

The motivation behind this project is to understand the non-covalent coupling of nanoparticles to graphene by the design of electron rich aromatic ring containing ligands, to achieve good coupling with graphene and the designed ligands, to understand the ligand interaction with graphene surface, and the applications of the produced nanocomposites. Small molecule ligands as well as polymeric ligands have been investigated.

**3. Results and Discussion**

In this project, we report on the synthesis and characterization of novel graphene-iron oxide hybrid systems which was accomplished through the creative anchoring way for the magnetic iron-oxide nanoparticles with desired chemistry for the adsorption of pyrene to the graphene nanosheets as shown in Scheme 1. The detailed synthetic methods and characterizations are given in this section.



Scheme 1. Synthetic routes of target molecular systems with magnetic functions

### 3.1. Pyrene-Spacer-Dopamine (PyDop) Ligands

The central theme of research done by the Korean PI revolves around designing of amphiphilic ligand systems capable of coupling graphene with magnetic nanoparticles. The nonpolar surface of graphene could be addressed by a pyrene anchor while the oxidic surface of magnetic nanoparticles (MNP) can be addressed by the catechol moiety in dopamine. Ligands of various spacer lengths were designed in order to investigate the effect of spacing between the MNPs and graphene on the magnetic and electronic properties of the latter. The pyrene-spacer-dopamine (PyDop) ligands can be described by their spacing length defined as the distance between the connection at pyrene and the hydroxyl group on dopamine. The ligands investigated during this project along with their spacing lengths can be seen in Figure 1. Ligands PyDop1 and PyDop2 are small molecule ligands, while polymeric ligand (PyDop3) constitute a dopamine end functionalized block copolymer with multiple pyrene anchoring unit.

The synthesis of PyDop1 ligand was reported in the first year report. Many difficulties were encountered during the scale of the molecule because it involves a total of five steps with two low yielding final steps. A new reaction route was developed for synthesizing PyDop1 as seen in Scheme 2. Previously reported route 1 involved the five step synthesis of dopamine with protective functionalization at the catechol moiety. The subsequent amidation reaction proceeded at low yields. This affected the overall efficiency of the reaction resulting in very low yields of PyDop1. Alternatively we developed route 2 constituting 3 steps that follows the formation of a parafluorobenzene active ester perfluorophenyl 4-(pyren-4-yl)butanoate. A simple room temperature reaction under mild basic conditions yields the coupling of dopamine from dopamine hydrochloride with perfluorophenyl-4-(pyren-4-yl)butanoate. Active ester reacted with dopamine hydrochloride to yield the final product at a moderate yield of 40%

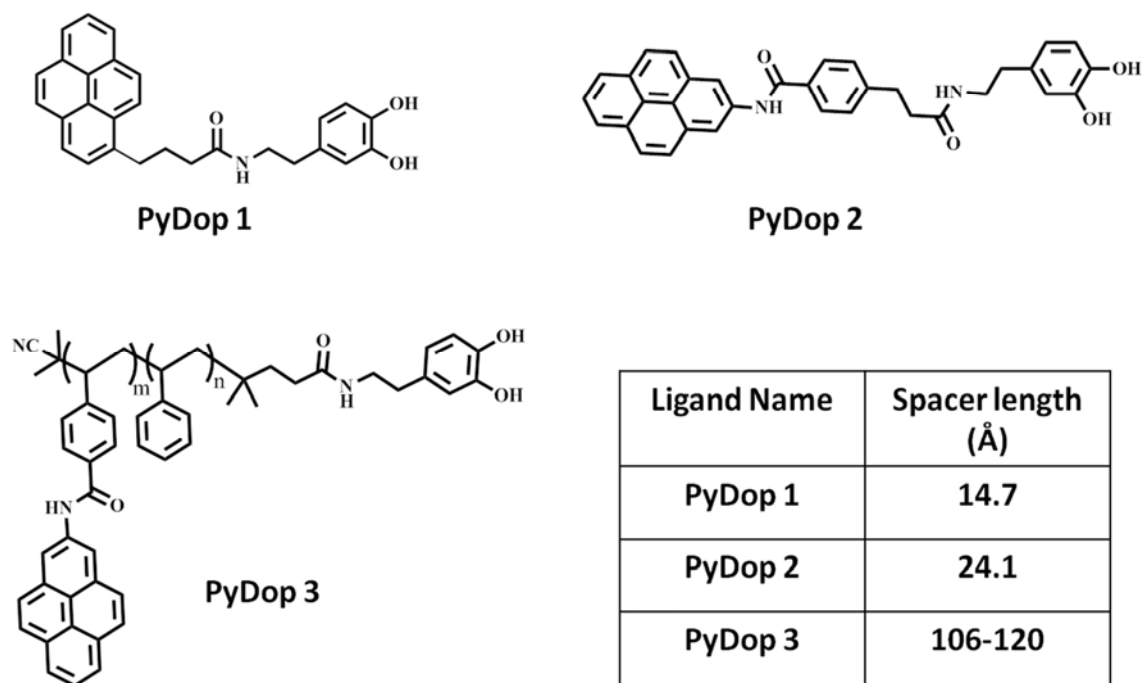
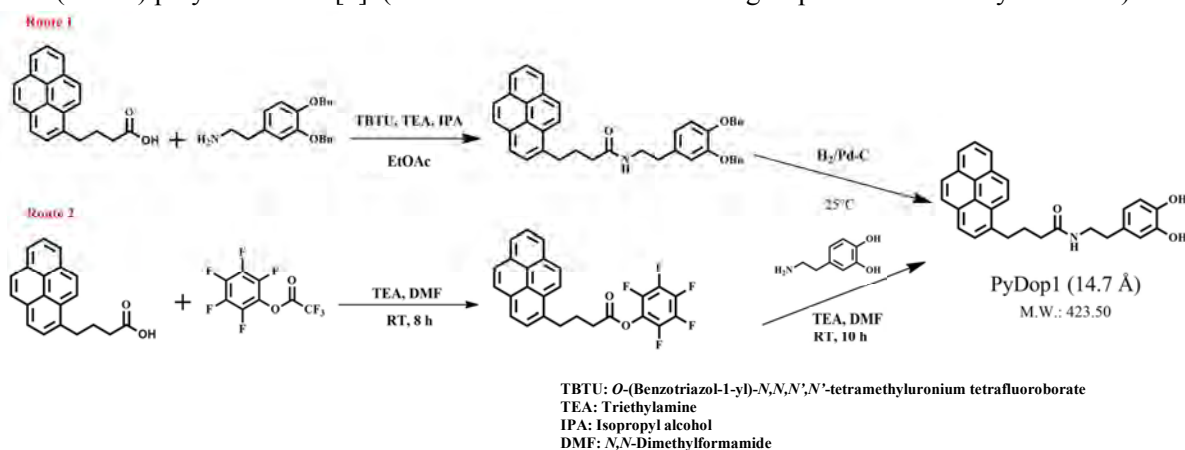
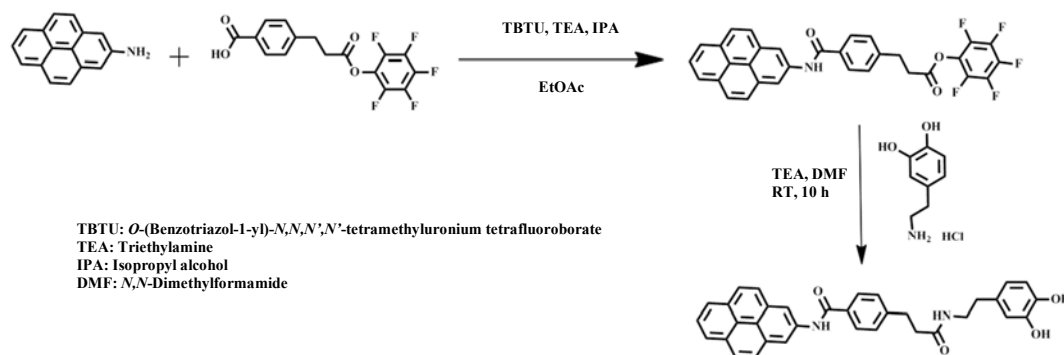


**Figure 1.** PyDop Ligands designed and investigated during our studies. The spacing between the magnetic nanoparticle and the pyrene group ranges from 14.7 Å to 120 Å. The spacing lengths of the small molecule ligands PyDop1 and PyDop2 as well as a multianchor block copolymer ligand PyDop3 are summarized in the table.

which was better than route 1. Ligand PyDop2 and PyDop3 were also synthesized through parafluorobenzene active ester chemistry. The ligand PyDop2 was synthesized as shown in Scheme 3. Both PyDop 1 and 2 are small molecule ligands with single tethering group for graphene surface. The third ligand PyDop3 ( $m \approx 6$ ,  $n \approx 18$ ) which is a dopamine end-functionalized styrene-co-(*N*-(perfluorophenyl)-4-vinylbenzamide) block copolymer was synthesized by reversible addition fragmentation transfer (RAFT) polymerization [6]. (coworked with Prof. R. Zentel group at the University of Mainz).



**Scheme 2.** Two different synthetic routes for PyDop1



**Scheme 3.** Synthetic route of PyDop2

### 3.2 Synthesis of Superparamagnetic $\gamma$ -Fe<sub>2</sub>O<sub>3</sub> Nanoparticles

Monodisperse superparamagnetic iron oxide ( $\gamma$ -Fe<sub>2</sub>O<sub>3</sub>) nanoparticles were synthesized by the thermal decomposition of iron-oleate complex followed by the air oxidation by trimethylamine *N*-oxide to give superparamagnetic nanoparticles following reported procedures [7]. The ratio between the iron precursor and the ligand oleic acid controls the size of the MNPs during the formation and decomposition of the iron-oleate complex. Greater ratio of oleic acid leads to larger nanoparticles. A 1:1 ratio of iron precursor to oleic acid yielded monodisperse nanoparticles of 5-7 nm.

### 3.3 Coupling $\gamma$ -Fe<sub>2</sub>O<sub>3</sub> Nanoparticles with Ligands

At the end of the nanoparticle synthesis, oleic acid coupled  $\gamma$ -Fe<sub>2</sub>O<sub>3</sub> nanoparticles dispersions are obtained in hexane. The nanoparticles can be precipitated by centrifugation of the hexane dispersion at 4000 rpm for 6 min, followed by decantation of the supernatant. An alternative method is to use a magnet to induced magnetic aggregation of nanoparticles followed by decantation of supernatant hexane. The nanoparticle can be dispersed by adding a solvent and sonicating for 10 min. Ligand exchange with PyDop1 can be carried out either in hexane or THF.

The oleic acid ligand on  $\gamma$ -Fe<sub>2</sub>O<sub>3</sub> can be replaced by PyDop1 by a simple sonication procedure carried out in tetrahydrofuran (THF). In a typical procedure 40 mg  $\gamma$ -Fe<sub>2</sub>O<sub>3</sub> and 2 mg PyDop1 is taken in 5 ml THF and sonicated for 1 hour. The amount of ligand required for coupling with nanoparticles were calculated by taking into account the size of MNPs, their surface area as well as the surface area occupied by single catechol moiety in dopamine. The coupling of the ligand with MNP can be followed by FT-IR spectrum as shown in Figure 2. The resultant nanohybrid PyDop1- $\gamma$ -Fe<sub>2</sub>O<sub>3</sub> shows characteristic peaks of PyDop1 ligand peaks. The spectra show slight variation depending on the processing conditions. FT-IR measurements were carried out by making KBr pellets containing small amounts of material to be analyzed. The ligand PyDop1 exhibits peaks at 3280 (-OH), 3300 (-NH-), 3100 (-NH-) bending overtone, 2780 (=C-H), 1736 (C=O). Effective coupling of ligand with nanoparticle should leads to a self-assembled layer of about a molecule thickness on the surface of  $\gamma$ -Fe<sub>2</sub>O<sub>3</sub>. The low concentration ligands present on the nanoparticle thus gives spectra far weaker than the ligand only sample seen in Figure 2. The spectrum compares the ligand PyDop1 with PyDop1- $\gamma$ -Fe<sub>2</sub>O<sub>3</sub> prepared in hexane and THF. From the comparison the decreased intensity of the -OH, -NH and -C=O is markedly decreased in the PyDop1- $\gamma$ -Fe<sub>2</sub>O<sub>3</sub>, a close examination reveals small peaks in these regions. The shape of the hydroxyl peak in the ligand exchanged nanoparticles is changed as expected due to their interaction with the oxidic surface of the MNP.



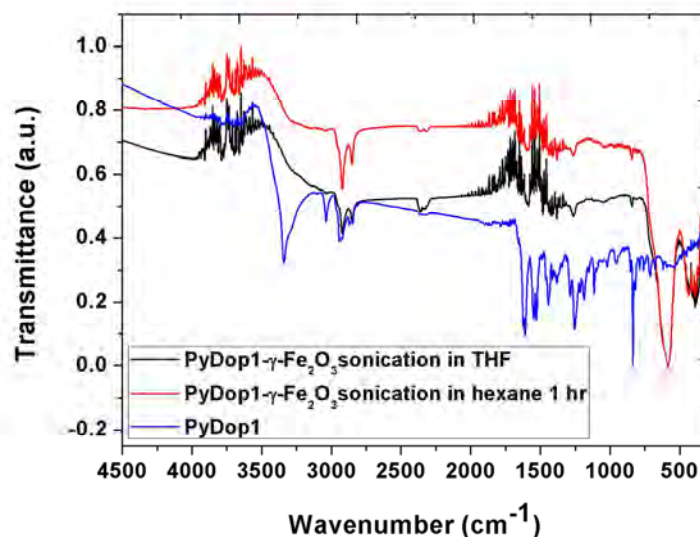


**Figure 2.** IR spectra of PyDop1 and coupled compounds of PyDop2 with  $\gamma\text{-Fe}_2\text{O}_3$  in THF and hexane.

Alternatively the ligand exchange can be carried out by shaking the ligands and the nanoparticles in a solvent for two or three days. The shaking-based ligand exchange gave slightly better results, we are in the process of evaluating the influence of synthetic method on nanocomposite formation and properties. To couple PyDop2 to  $\gamma\text{-Fe}_2\text{O}_3$ , 0.087 mg of the ligand was treated with 4 mg of oleic acid functionalized nanoparticles. The ligand exchange was carried out by sonicating the ligand and the nanoparticles in THF. The ligand exchange can be followed by UV-Vis spectroscopy. Pyrene in PyDop ligands exhibit a distinctive UV peak between 300-390 nm. The appearance of this peak in the nanoparticle spectrum indicates the successful coupling of the PyDop2 ligand on to  $\gamma\text{-Fe}_2\text{O}_3$ . The UV spectra are summarized in Figure 3. To make PyDop3 functionalized magnetic nanoparticles, 0.079 mg of the ligand PyDop3 was treated with 4 mg of oleic acid functionalized  $\gamma\text{-Fe}_2\text{O}_3$  nanoparticles in THF. The coupling of the ligand onto the nanoparticle can be UV-Vis spectroscopy, Figure 4. In both UV-visible spectra, a distinctive absorptions of pyrene can be seen even after coupling of MPs at the dopamine functional groups. In these cases, a blue shifted UV absorption of pyrene was observed by the interaction with MPs.

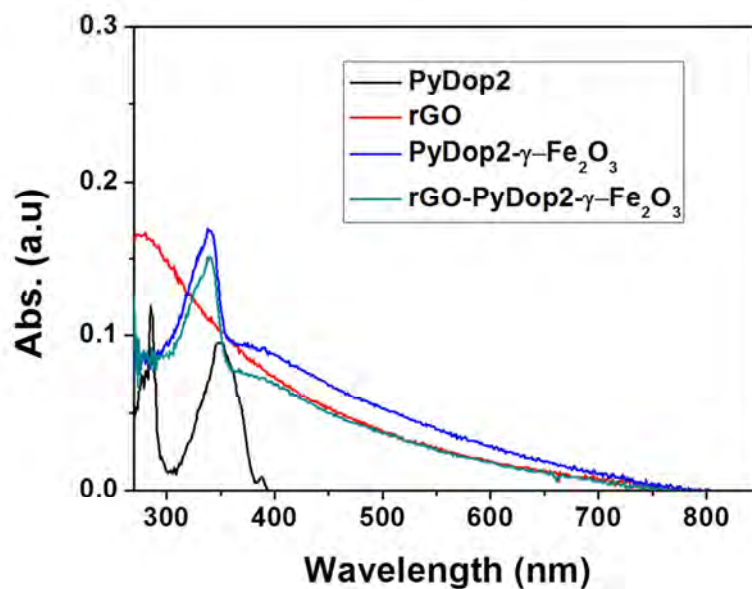


**Figure 3.** UV spectra of PyDop2, PyDop2- $\gamma$ -Fe<sub>2</sub>O<sub>3</sub> and GNP-PyDop2- $\gamma$ -Fe<sub>2</sub>O<sub>3</sub>. The distinctive pyrene peak between 300-390 nm can be seen in both PyDop2- $\gamma$ -Fe<sub>2</sub>O<sub>3</sub> and GNP-PyDop2- $\gamma$ -Fe<sub>2</sub>O<sub>3</sub>. In the graph please read rGO as (GNP).

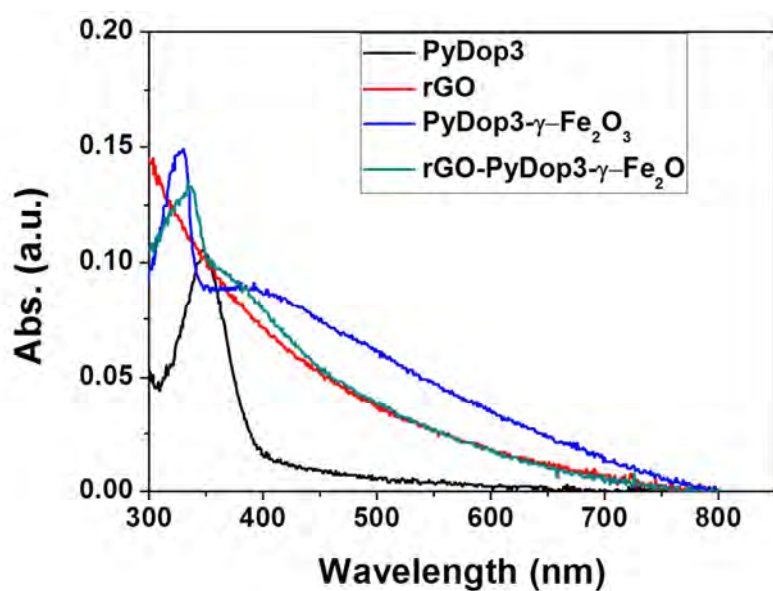


**Figure 4.** UV spectra of PyDop3, PyDop3- $\gamma$ -Fe<sub>2</sub>O<sub>3</sub> and GNP-PyDop3- $\gamma$ -Fe<sub>2</sub>O<sub>3</sub>. The distinctive pyrene peak between 300-390 nm can be seen in both PyDop3- $\gamma$ -Fe<sub>2</sub>O<sub>3</sub> and GNP-PyDop3- $\gamma$ -Fe<sub>2</sub>O<sub>3</sub>. In the graph please read rGO as (GNP).

### 3.4. Coupling PyDop- $\gamma$ -Fe<sub>2</sub>O<sub>3</sub> Nanoparticles with Graphene Derivatives

Coupling  $\gamma$ -Fe<sub>2</sub>O<sub>3</sub> nanoparticles functionalized by PyDop ligands to graphene is essentially a process of self-assembly. The nanoparticles and graphene are dispersed in same or miscible solvents. The two materials are brought together by gradual mixing taking into consideration the kinetic cohesive aggregation that could happen when a high local concentration of any particular material is created. An ideal experiment involves a dilute dispersion of graphenic material to which the functionalized MNPs are added in small quantities over a period of time followed by sonication or shaking. The concentration of the functionalized MNPs should also be kept low so as to avoid aggregation between nanoparticles.

There are many ways to synthesize graphene which includes micromechanical exfoliation of graphite, chemical vapour deposition, epitaxial growth on electrically insulating surface, liquid phase and electrochemical exfoliation of graphite and graphite intercalation compounds, chemical reduction of graphene oxide or graphite oxide, etc [3]. So far we have used graphene sheets obtained from three different synthetic methods: (i) electrochemical exfoliation of highly oriented pyrolytic graphite (HOPG) [8], (ii) reduction of graphene oxide by phenyl hydrazine [9], and (iii) graphene nanoplatelets stabilized by graphene oxide [10].

#### 3.4.1. PyDop1- $\gamma$ -Fe<sub>2</sub>O<sub>3</sub>-GO/GNP Nanosheets

Graphene nanoplatelets (GNPs) stabilized by graphene oxide (GO) prepared by following the previously reported procedures [10,11] are used to couple PyDop1- $\gamma$ -Fe<sub>2</sub>O<sub>3</sub>. GNPs provide the intrinsic graphene electrical conductivity to the GNP/GO films. The GNP/GO film is ultrasonicated in *N*-methylpyrrolidone (NMP) for 1 hour, and centrifuged to obtain a stable dispersion of GNP/GO sheets. This GNP/GO dispersion is further ultrasonicated with PyDop1- $\gamma$ -Fe<sub>2</sub>O<sub>3</sub> in THF, in a mass ratio of 1:4 in order to couple PyDop1- $\gamma$ -Fe<sub>2</sub>O<sub>3</sub> magnetic nanoparticles into GNP/GO sheets. Figure 5a represents the TEM image of GNP/GO-PyDop1- $\gamma$ -Fe<sub>2</sub>O<sub>3</sub> hybrid, which clearly displays uniform arrangement of PyDop1- $\gamma$ -Fe<sub>2</sub>O<sub>3</sub> magnetic nanoparticles on the surface of GNPs. The characteristic  $\gamma$ -Fe<sub>2</sub>O<sub>3</sub> lattice fringes are clearly visible in high-resolution transmission electron microscopic (HRTEM) image of GNP/GO - PyDop1- $\gamma$ -Fe<sub>2</sub>O<sub>3</sub> hybrid (Figure 5b), A live fast fourier transform (FFT) pattern (represented by blue dotted circle) is shown in Figure 5c, indicates the crystalline nature of the hybrid.

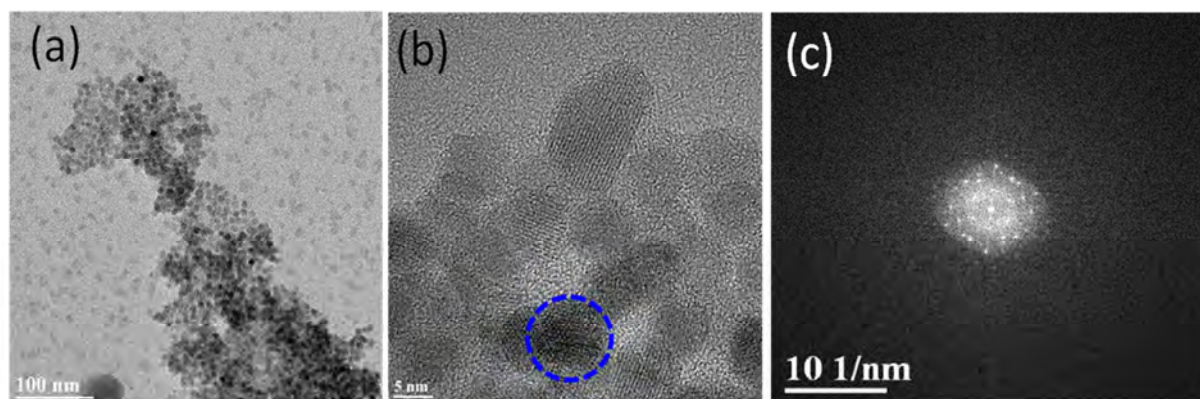


**Figure 5.** TEM images and FFT analysis from PyDop1-  $\gamma$ -Fe<sub>2</sub>O<sub>3</sub>. (a) and (b) progressive magnification of nanoparticles immobilized on GNP. (c) FFT on nanoparticle in the composite showing crystalline character .

#### 3.4.2. PyDop2- $\gamma$ -Fe<sub>2</sub>O<sub>3</sub>-GO/GNP Nanosheets

In the case of PyDop2- $\gamma$ -Fe<sub>2</sub>O<sub>3</sub>-GO/GNP nanosheets, the 4 mg of PyDop2 was reacted with 1 mg of graphene by sonication. The product can be seen in Figure 6. The exfoliation of GO/GP nanosheets yield smaller sheets of GO and GNPs. The MNPs can be seen attached in high densities on to the GNP sheets.

Figures 6a-c show progressively magnified images of nanoparticles assembled on GNP platelets. The FFT on top of the nanoparticle outlined blue in Figure 6c is given in Figure 6d. The FFT reveals crystalline domains whose lattices spacing values match that of  $\gamma\text{-Fe}_2\text{O}_3$ .

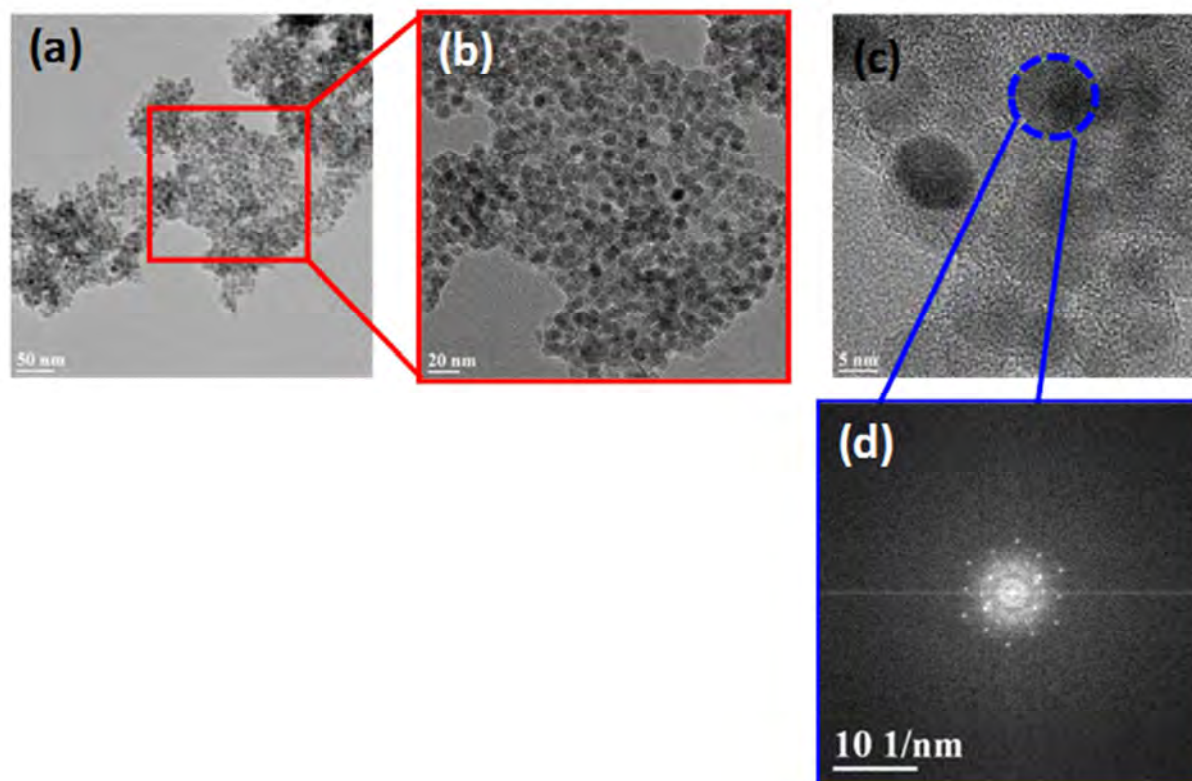


**Figure 6.** TEM images and FFT analysis from PyDop1- $\gamma\text{-Fe}_2\text{O}_3$ . (a)-(c) progressive magnification of nanoparticles immobilized on rGO platelet (d) FFT on nanoparticle in the composite showing crystalline character.

### 3.4.3. PyDop3- $\gamma\text{-Fe}_2\text{O}_3$ -GO/GNP Nanosheets

The polymeric PyDop3 functionalized PyDop2- $\gamma\text{-Fe}_2\text{O}_3$  presents multidentate ligands with multiple pyrene units per ligand unlike PyDop1 and PyDop2. To couple the nanoparticles to GNP or GO sheets 4 mg of the functionalized nanoparticles are sonicated together in NMP. TEM measurements after experiments reveal high density of MNPs on GNP surface. Apparently very large sheets of MNP coupled with GO was not obtained with this method, which is currently under investigation. So far we believe that hydrophilic GO is filtered out during ultrasonication and centrifugation in NMP. The role of the multidentate ligands on the nanoparticle will be thoroughly investigated in our ongoing studies. The pyrene groups are sticky for each other and for the conjugated pane of GNP. It would be interesting to see how the association between different materials are evolving with changing concentration of PyDop2- $\gamma\text{-Fe}_2\text{O}_3$ . The results from TEM images can be seen in Figure 7. The FFT on the nanoparticles immobilized on GNP reveals lattice spacing corresponding to  $\gamma\text{-Fe}_2\text{O}_3$ .



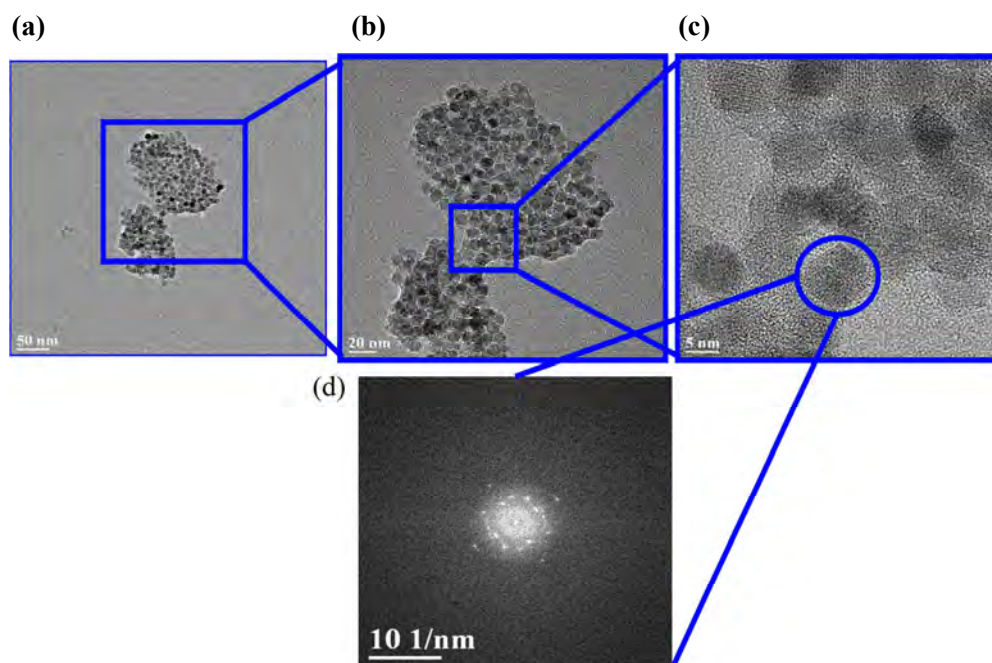


**Figure 7.** TEM images and FFT analysis from PyDop3- $\gamma$ -Fe<sub>2</sub>O<sub>3</sub>. (a)-(c) progressive magnification of nanoparticles immobilized on GNP, (d) the lattice spacing gives by FFT analysis on the nanoparticle in a blue circle in (c) gives lattice values corresponding to  $\gamma$ -Fe<sub>2</sub>O<sub>3</sub>.

#### 3.4.4. PyDop1- $\gamma$ -Fe<sub>2</sub>O<sub>3</sub>-Graphene Sheets

Graphene sheets are obtained from electrochemical exfoliation of highly oriented pyrolytic graphite (HOPG) flake. Two electrode system containing platinum as counter electrode and HOPG as working electrode is employed with aqueous H<sub>2</sub>SO<sub>4</sub> electrolyte. When a direct current voltage is applied to HOPG electrode, the HOPG flakes starts to exfoliate and disperse into electrolyte solution. On completion of exfoliation process, the exfoliated graphene sheets are collected by vacuum filtration and repeatedly washed away any residual salts. The collected exfoliated graphene are further ultrasonicated in NMP, and centrifuged to remove any unexfoliated products. The well dispersed and stable graphene sheets in NMP are collected and coupled with PyDop1- $\gamma$ -Fe<sub>2</sub>O<sub>3</sub> nanoparticles with the aid of ultrasonication.

HRTEM images indicates that the obtained graphene sheets range from single layer to few layers, Figure 8a and 8b. The selected area electron diffraction (SAED) pattern in Figure 8b exhibits a typical 6-fold symmetric diffraction of (110) basal plane of graphene sheet. HRTEM images of PyDop1- $\gamma$ -Fe<sub>2</sub>O<sub>3</sub>-graphene hybrid is presented in Figure 8c-d. As shown, PyDop1- $\gamma$ -Fe<sub>2</sub>O<sub>3</sub> nanoparticles are distributed densely in an inhomogenous manner all over the graphene sheet. In Figure 8d, the characteristic lattice fringes of  $\gamma$ -Fe<sub>2</sub>O<sub>3</sub> nanoparticles in graphene sheet is shown. Typical X-ray diffraction (XRD) patterns of the HOPG, exfoliated graphene, PyDop1- $\gamma$ -Fe<sub>2</sub>O<sub>3</sub> and PyDop1- $\gamma$ -Fe<sub>2</sub>O<sub>3</sub>-graphene are given in Figure 1e. HOPG show a very sharp diffraction peak at 26.5° corresponding to a d-spacing of 0.31 nm (*d*<sub>002</sub>), which disappeared in the XRD pattern of graphene sheet indicating effective exfoliation. The diffraction peaks of PyDop1- $\gamma$ -Fe<sub>2</sub>O<sub>3</sub> and graphene-PyDop1- $\gamma$ -Fe<sub>2</sub>O<sub>3</sub> are coincided well with the standard data of  $\gamma$ -Fe<sub>2</sub>O<sub>3</sub> (JCPDS no. 39-1346) which is also included in Figure 8e.

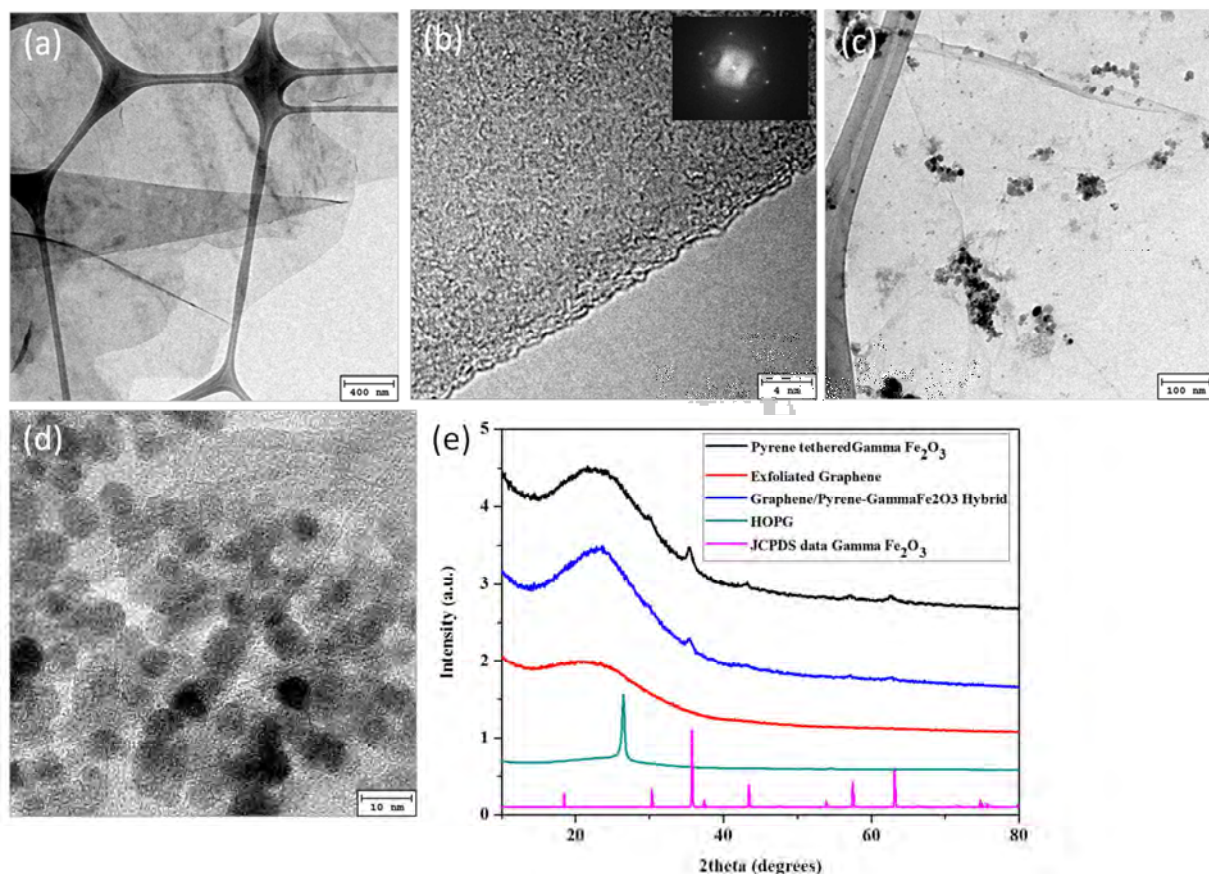


**Figure 8.** (a) TEM image of exfoliated graphene sheets, (b) HRTEM image of edge of graphene sheet, inset is SAED pattern indicating six spots corresponding to carbon atoms arranged in hexagonal pattern in honey comb crystal lattice, (c) TEM (d) HRTEM image of graphene-PyDop1-MNP hybrid, (e) XRD pattern of the HOPG, exfoliated graphene, PyDop1-MNP, graphene-PyDop1-MNP and standard pattern of  $\gamma$ - $\text{Fe}_2\text{O}_3$  from JCPDS No. 39-1346 is also given in (e).

### 3.4.5. PyDop1- $\gamma$ - $\text{Fe}_2\text{O}_3$ -Chemically Converted Graphene

Graphene oxide is chemically reduced into graphene (CCG) with phenyl hydrazine in room temperature. The CCG is redispersed in NMP by ultrasonication for 1 hour. HRTEM image of CCG is given in Figure 9a, which shows exfoliated graphene sheets with edges inwards. The stable dispersion of CCG in NMP is coupled with PyDop1- $\gamma$ - $\text{Fe}_2\text{O}_3$  in THF with the aid of ultrasonication in a weight ratio of CCG to PyDop1- $\gamma$ - $\text{Fe}_2\text{O}_3$  as 1:4. Figure 9b-c represents the HRTEM image of PyDop1- $\gamma$ - $\text{Fe}_2\text{O}_3$ -CCG hybrid. The uniformly sized PyDop1- $\gamma$ - $\text{Fe}_2\text{O}_3$  magnetic nanoparticles are found uniformly distributed on the surface of CCG. Inset of Figure 9c is the corresponding SAED pattern and displayed the crystalline nature of PyDop1- $\gamma$ - $\text{Fe}_2\text{O}_3$ -CCG hybrid. Figure 9d presents the dispersive X-ray analysis (EDS) spectrum. As shown, the EDS spectrum shows carbon as major concentration, and iron and oxygen elements in 2: 3 ratio which indicated that the sample contains almost pure  $\text{Fe}_2\text{O}_3$ .

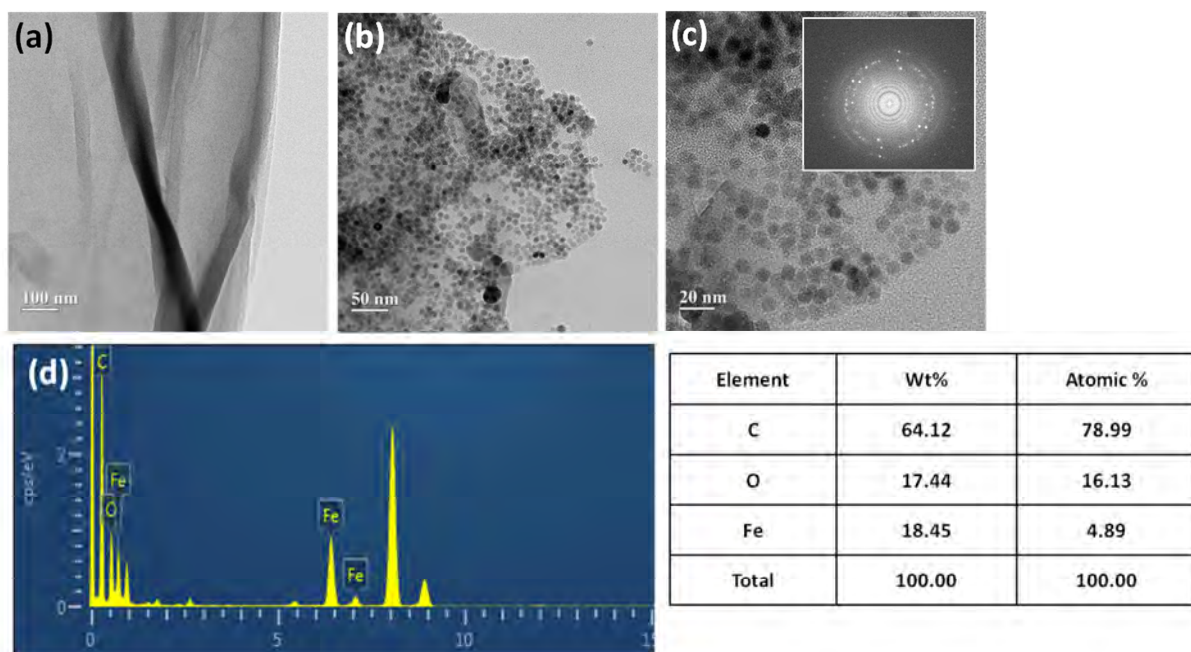


**Figure 9.** HRTEM images of (a) CCG, (b-c) graphene-PyDop1- $\gamma$ -Fe<sub>2</sub>O<sub>3</sub> hybrid, Inset in (c) is SAED pattern, (d) EDS spectra of PyDop1- $\gamma$ -Fe<sub>2</sub>O<sub>3</sub>-CCG hybrid, atomic percentage of C, O and Fe is on the right.

### 3.5 Tunable Memories with PyDop1- $\gamma$ -Fe<sub>2</sub>O<sub>3</sub>-Graphene Oxide Charge Trapping Layer

Organic memory transistors offer a promising alternative to more traditional memory elements such as polysilicon and silicon nitride based memory transistors due to their advantages related to rapid processing, potential low cost, ability to cater performance and properties through molecular design, and compatibility with flexible electronics. A physical memory is created in a transistor when a charge created under an applied bias is stored within a device. The charge is stored inside a transistor stack. A memory cell is typically comprised of a charge trapping layer sandwiched between a main dielectric and a thin barrier dielectric. Under an applied bias, charge can be transferred into the charge trapping layer through the thin barrier dielectric. A typical organic memory device can be seen in Figure 10a. The mechanism for which charge injection occurs varies based on device architecture, however, examples include Fowler-Nordheim tunneling and avalanche break down [12]. Progress in organic memory transistors has moved rapidly with an emphasis placed on enabling flexible and low-voltage operation [13, 14]. Additionally, the exploration of potentially new charge trapping materials and tunable memory effects remains a priority. Recent studies have established graphene oxide as a promising charge trap layer [15]. Tunable memory devices have been demonstrated by doping utilizing a reduced graphene oxide memory charge trapping layer by controlled doping with gold chloride [16].

The possibility of creating tunable memories with PyDop1- $\gamma$ -Fe<sub>2</sub>O<sub>3</sub> as a charge trap layer was examined in collaboration with Prof. Alex. K.-Y. Jen. Initial experiments were carried out to demonstrate the proof of concept. The work would be extended by systematically studying the influence of applied external magnetism on tuning the memory storage. *Guo et. al* has recently showed that a graphene oxide-magnetic iron oxide nanoparticle could vastly increased capacitance under an applied magnetic field [17].



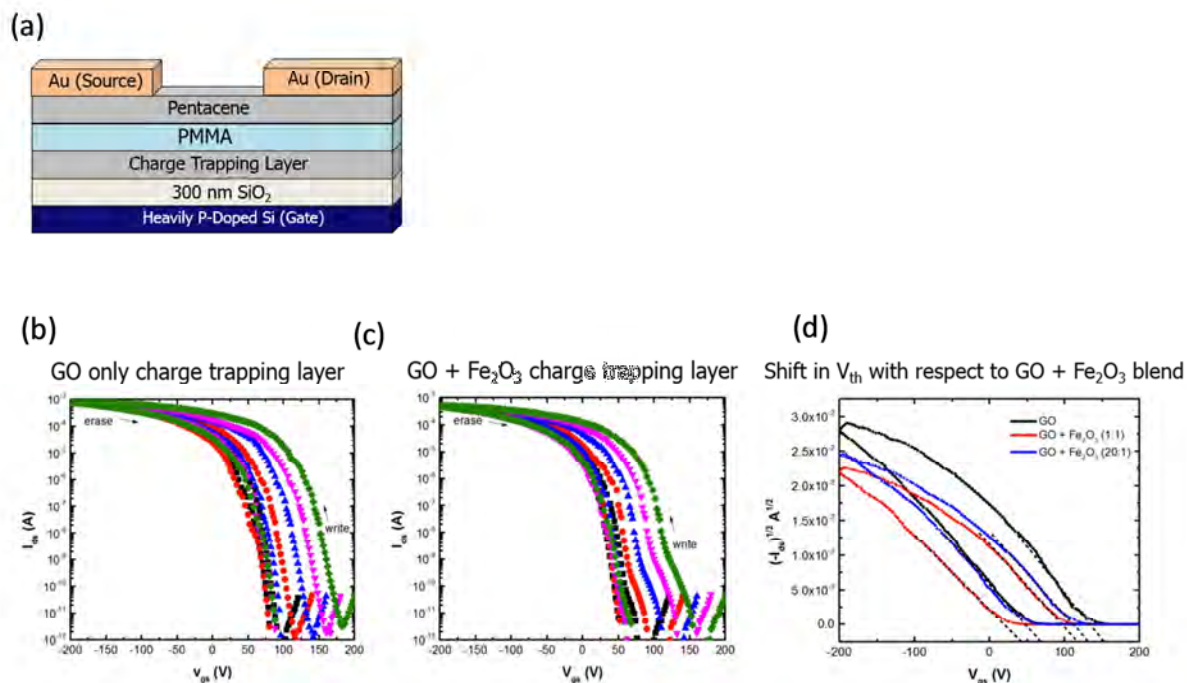


**Figure 10.** (a) Device architecture of organic memory transistor utilizing charge trapping layer mechanism for memory effect. Representative transfer curves of organic memory transistors with (b) graphene oxide only and (c) blended 1:1 ratio by volume of graphene oxide and PyDop1 charge trapping layer (d) shift in threshold voltage based on different blends of graphene oxide and PyDop1 iron oxide nanoparticles.

A PyDop1- $\gamma$ -Fe<sub>2</sub>O<sub>3</sub>-graphene oxide (GO) composite was used as a charge trapping layer inside a memory transistor. The combination PyDop1- $\gamma$ -Fe<sub>2</sub>O<sub>3</sub>-GO composite could be used to create a hybrid charge trapping layer and the assembled iron oxide nanoparticles can be used to control the overall capacitance of this system under an applied magnetic field. Figure 10b-c compares the memory transistor effect in a device containing a GO charge trap layer and another that uses PyDop1- $\gamma$ -Fe<sub>2</sub>O<sub>3</sub>-GO as a charge transfer layer. Preliminary results show replication of a memory transistor with a graphene oxide charge trapping layer. A representative transfer curve under different applied gate-source biases can be seen in Figure 10b. A clear memory effect is seen with the hysteresis changing under an applied bias. Attempts have been made to modify the charge trapping layer by fabricating alternating stacks of GO and PyDop1, however, due to surface energy mismatch it is difficult to fabricate a secondary layer of graphene oxide on top of the nanoparticles. Additional experiments are needed in order to determine a viable way to fabricate alternating stacks of these two materials.

In order to overcome this issue quickly and determine if there is any influence of the iron oxide nanoparticles on the memory characteristics of these transistors, a blended PyDop1- $\gamma$ -Fe<sub>2</sub>O<sub>3</sub> and GO charge trapping layer has been fabricated. Different blending ratios of 1:1 and 20:1 of graphene oxide and PyDop1 have been tested. From the transfer curve in Figure 10c, a clear difference in threshold voltage can be seen with the turn on voltage shifting significantly towards 0 volt. This shift in threshold voltage may be related to iron oxide influencing the work function of graphene oxide. However, further studies are necessary in order to elucidate the exact mechanism. Figure 10d shows a clear shift of threshold voltage, in addition to a slight change in memory window. The magnitude of change in memory window is difficult to determine due to device variation, however after additional statistical studies it should become apparent.



#### 4. Conclusions

- Pyrene-Spacer-Dopamine (PyDop) ligands with different spacer lengths were synthesized.
- Monodisperse  $\gamma$ -Fe<sub>2</sub>O<sub>3</sub> nanoparticles stabilized with the PyDop ligands using either sonication or shaking.
- Graphene based materials were obtained by exfoliation of graphene nanoplatelet-graphene oxide paper, chemically reduced graphene or by electrochemical exfoliation of graphene.
- The graphene based materials were coupled with the ligands by self-assembly in a mutually soluble solvent or solvent mixture
- The TEM analysis of graphene-MNP nanocomposites revealed highly dense packing of nanoparticles on the surface of graphene.
- MNP spaced with short ligand on top of graphene has been used as a charge trap layer in a memory transistor device
- The control of self-assembly of MNPs on graphene is being studied in thorough detail.
- Statistical analysis of memory transistors are being conducted to understand the memory effect.

#### 5. Reference

- [1] M. Xu, T. Liang, M. Shi, H. Chen, *Chem. Rev.* **2013**, *113*, 3766.
- [2] K. S. Novoselov, V. Fal, L. Colombo, P. Gellert, M. Schwab, K. Kim, *Nature* **2012**, *490*, 192.
- [3] S. Park, R. S. Ruoff, *Nature Nanotech.* **2009**, *4*, 217.
- [4] Y. Zhang, L. Zhang, C. Zhou, *Acc. Chem. Res.* **2013**, *46*, 2329.
- [5] V. Georgakilas, M. Otyepka, A. B. Bourlinos, V. Chandra, N. Kim, K. C. Kemp, P. Hobza, R. Zboril, K. S. Kim, *Chem. Rev.* **2012**, *112*, 6156.
- [6] F. Mathias, M. N. Tahir, W. Tremel, R. Zentel, *Macromol. Chem. Phys.* **2014**, *215*, 604.
- [7] T. Hyeon, S. S. Lee, J. Park, Y. Chung, H. B. Na, *J. Am. Chem. Soc.* **2001**, *123*, 12798.
- [8] K. Parvez, Z.-S. Wu, R. Li, X. Liu, R. Graf, X. Feng, K. Müllen, *J. Am. Chem. Soc.* **2014**, *136*, 6083.
- [9] V. H. Pham, T. V. Cuong, T.-D. Nguyen-Phan, H. D. Pham, E. J. Kim, S. H. Hur, E. W. Shin, S. Kim, J. S. Chung, *Chem. Commun.* **2010**, *46*, 4375.
- [10] D. Y. Kim, M. Kim, D. W. Kim, J. Suk, O. O. Park, Y. Kang, *Carbon* **2015**, *93*, 625.
- [11] M. Kim, D. Y. Kim, Y. Kang, O. O. Park, *RSC Advances* **2015**, *5*, 3299.
- [12] S. Sie, "Physics of Semiconductor Devices, (1981)", John Wiley & Sons, New York.
- [13] C. Kim, J.-M. Song, J.-S. Lee, M. J. Lee, *Nanotechnology* **2014**, *25*, 014016.
- [14] T. Sekitani, T. Yokota, U. Zschieschang, H. Klauk, S. Bauer, K. Takeuchi, M. Takamiya, T. Sakurai, T. Someya, *Science* **2009**, *326*, 1516.
- [15] T.-W. Kim, Y. Gao, O. Acton, H.-L. Yip, H. Ma, H. Chen, A. K.-Y. Jen, *Appl. Phys. Lett.* **2010**, *97*, 023310.
- [16] S.-T. Han, Y. Zhou, Q. D. Yang, L. Zhou, L.-B. Huang, Y. Yan, C.-S. Lee, V. A. Roy, *ACS Nano* **2014**, *8*, 1923.
- [17] J. Zhu, M. Chen, H. Qu, Z. Luo, S. Wu, H. A. Colorado, S. Wei, Z. Guo, *Energy Environ. Sci.* **2013**, *6*, 194.

**Prof. Alex K.-Y. Jen (USA PI)**

**“Tunable Memory Characteristics of Self-Assembled Monolayer Transistors via Interlayered Magnetic Nanoparticle and Graphene Oxide Charge Trapping Layer”**

**1. Abstract**

Low voltage self-assembled monolayer field-effect transistors (SAMFETs) that operate under an applied bias of less than -3 V and a high hole-mobility of  $10^{-2} \text{ cm}^2 \text{ V}^{-1} \text{ s}^{-1}$  are reported. A self-assembled monolayer (SAM) with a quaterthiophene semiconducting core and a phosphonic acid binding group is used to fabricate SAMFETs on both high-voltage ( $\text{AlO}_x/300 \text{ nm SiO}_2$ ) and low-voltage ( $\text{HfO}_2$ ) dielectric platforms. High performance is achieved through the enhanced SAM packing density via a heated assembly process and through the improved electrical contact between SAM semiconductor and metal electrodes. Enhanced electrical contact is obtained by utilizing a functional methyl-thio head group combined with thermal annealing post gold source/drain electrode deposition to facilitate the interaction between SAM and electrode. Furthermore, this SAMFET platform will be utilized as a monolayer memory transistor that has a charge trapping layer comprised of an interlayered magnetic nanoparticles and graphene oxide.

**2. Introduction**

**2.1. Background**

Organic memory transistors offer a promising alternative to more traditional memory elements such as polysilicon and silicon nitride based memory transistors due to their advantages related to rapid processing, potential low cost, ability to cater performance and properties through molecular design, and compatibility with flexible electronics. For the purpose of this study, organic memory transistors operate with a similar mechanism to traditional inorganic nonvolatile memory transistors which achieve a memory effect via charge storage that is created under an applied bias [1]. Principally this charge storage mechanism is enabled through the use of a memory cell which is integrated within the transistor stack. A memory cell is typically comprised of a charge trapping layer sandwiched between a main dielectric and a thin barrier dielectric. Under an applied bias, charge can be transferred into the charge trapping layer through the thin barrier dielectric. The mechanism for which charge injection occurs varies based on device architecture, however, examples include Fowler-Nordheim tunneling and avalanche break down [2].

Progress in organic memory transistors has moved rapidly with an emphasis placed on enabling flexible and low-voltage operation. For example, *Lee et. al* has developed a process to achieve all solution processed memory transistors utilizing reduced graphene oxide as a charge trapping material on a flexible substrate with solution processed dielectric, electrodes, and semiconductor [3]. While *Someya et. al* has fabricated a floating gate memory transistor that uses a metal oxide and self-assembled monolayer hybrid dielectric stack to achieve flexible low voltage operation for use as a pressure sensor [4].

Additionally, the exploration of potentially new charge trapping materials and tunable memory effects remains a priority. *Kim et. al* has shown that graphene oxide is a promising material to act as a charge trap layer in memory transistors [5]. Which has been followed further by others and shown that reduced graphene oxide is also a viable charge trapping element [6]. Tuning the memory characteristics of these devices also remains critical in order enable the use of memory transistors in multioperational mode circuits. It has been shown that it is possible to tune memory characteristics of transistors utilizing a reduced graphene oxide memory charge trapping layer by controlled doping with gold chloride [7].

However, to date few studies have been completed examining the impact of a monolayer semiconductor in memory transistors. Promising results have been found with the metal dichalcogenide  $\text{MoS}_2$  which has been found to exhibit a significantly increased memory window as the number of  $\text{MoS}_2$  layers decreases [8]. Yet, quality  $\text{MoS}_2$  is acquired using exfoliation, a technique that has limited commercial viability.

Rather than using a difficult to obtain material such as MoS<sub>2</sub>, an alternative organic self-assembled monolayer semiconductor has been developed. A transistor with a semiconducting SAM is known as a self-assembled monolayer field-effect transistors (SAMFETs) which are a promising concept that uses rationally designed  $\pi$ -conjugated SAMs as the semiconductor of a transistor [9-13]. This concept works in principle because charge transport in an organic semiconductor based FET occurs in the first few monolayers closest to the dielectric [14-15]. SAMFETs are believed to have a broad appeal for organic semiconductor device applications due to their low-cost processing, reduced material quantity needed compared to traditional organic thin film transistors and ability to be used toward flexible electronics and sensing applications.

## 2.2. Motivation

One potential mechanism to enable the ability to tune the memory characteristics of SAMFETs is to use a hybrid nanocomposite charge storage layer. This charge storage layer would consist of a graphene based charge trapping element such as reduced graphene oxide or graphene oxide and a magnetic iron oxide nanoparticle. *Guo et. al* has recently showed that such a nanocomposite can have vastly increased capacitance under an applied magnetic field [16]. If such a system were applied to the charge storage layer of a self-assembled monolayer memory transistor, it would enable tuning of the memory characteristics with an applied magnetic field as capacitance is directly related to the amount of charge able to be stored.

The purpose of this research will be to examine the influence of a nanocomposite charge trapping layer in a self-assembled monolayer memory transistor that is comprised of graphene and iron oxide nanoparticles. This will be realizable through the following experimental studies:

- (1) Develop a high performance SAMFET platform that is able to achieve state of the art performance.
- (2) Determine the best architecture necessary to achieve high performance memory transistors based on a nanocomposite charge trapping layer.
- (3) Determine the influence of blend ratio between graphene and nanoparticle, whether performance is effected by blending or layered type architecture.
- (4) Once optimized conditions are found, explore the influence of a magnetic field on the memory characteristics of these memory devices.

If these experimental results can be achieved, this will allow for a way to tune the memory characteristics of an organic monolayer memory transistor with a simple magnetic field. Memory characteristics of already fabricated devices would be able to be adjusted without the need to physically make a new device with modified processing or architecture differences.

However, first the fundamental issue of achieving a high performance SAMFET platform must be addressed. In order to achieve further performance enhancement, it is critical to overcome a fundamental challenge of efficient contact between the metal source/drain electrodes and SAM semiconductor in SAMFET devices. Efficient contacts between SAM semiconductor and electrodes may have been enabled by Smits et al. through under-etching the electrodes allowing the SAM to form underneath or, as shown by Schmaltz et al., through utilizing a secondary SAM to elevate the electrodes to allow edge-on contact with the SAM semiconductor core [10-11]. However, these reports utilize cumbersome and complicated device architectures that may make SAMFETs less appealing towards commercialization. Furthermore, little work has been done to examine the impact of SAM processing on molecular packing density.

Herein we demonstrate top-contact bottom-gate low voltage p-type SAMFETs with a hybrid HfO<sub>2</sub> dielectric that operates under a bias of -3 V and has a charge carrier mobility of 10<sup>-2</sup> cm<sup>2</sup> V<sup>-1</sup> s<sup>-1</sup>. Charge carrier mobility of the SAMFET is increased by over two orders of magnitude through the designed functional SAM terminal group that enables efficient charge injection between metal electrode and SAM semiconductor in conjunction with optimized processing conditions to enhance SAM packing density.

### 3. Results and Discussion

The SAM molecules, (11-(5'''-(4-(methylthio)butyl)-[2,2':5',2'':5'',2'''-quaterthiophen]-5-yl)undecyl)-phosphonic acid (MTB4TC11) and (12-(5'''-(4-(methylthio)butyl)-[2,2':5',2'':5'',2'''-quaterthiophen]-5-yl)dodecyl)phosphonic acid (MTB4TC12), used in this study are designed in such a manner to promote efficient charge injection between the semiconducting core and chosen electrode. As shown in Figure 11a the molecule is comprised of a phosphonic acid binding group which allows for the covalent attachment to a variety of metal oxides [17]. A flexible undecyl or dodecyl spacer unit is chosen to promote self-assembly and optimal  $\pi$ - $\pi$  overlap due to its conformational freedom [18]. A quaterthiophene unit is chosen as the semiconducting core due to its proven ability to work as a semiconductor in both thin film and monolayer transistors [18-19]. Finally, to achieve efficient charge injection into the SAM a functional terminal group composed of methylthiobutyl is chosen. In order to enhance charge injection and minimize contact resistance, the terminal group is designed to take advantage of the well-known gold-sulfide coordinate bond that occurs between the two species [20]. In particular, methylsulfide has been used in the past as an anchoring group for molecular junctions due to its ability to electronically couple with gold [21]. To take advantage of this intimate contact, a simple top-contact bottom-gate transistor architecture is used, Figure 11b. This will simplify the device architecture compared to those reported for previous high performance SAMFETs [10-11].

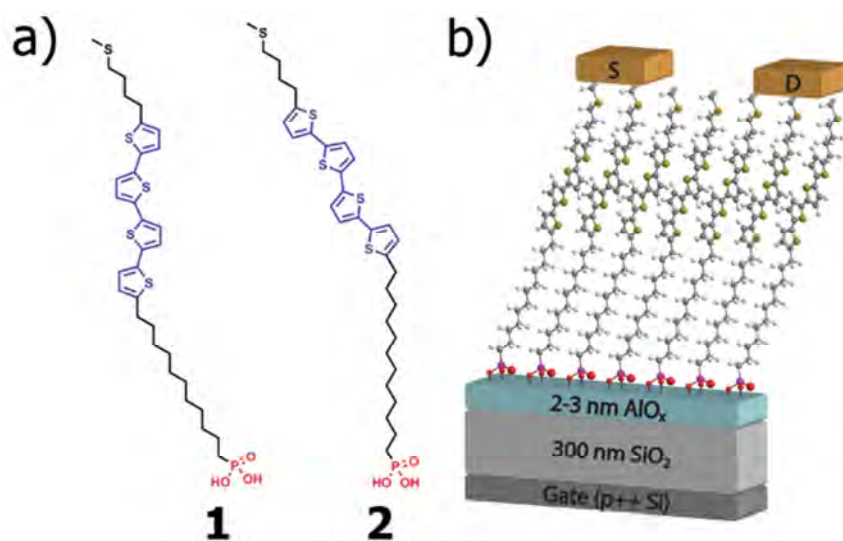


**Figure 11.** (a) Molecular structures of SAM semiconductors used in this study, **1** MTB4TC11 and **2** MTB4TC12; b) schematic of high-voltage SAMFETs fabricated.

In order to better understand the dynamics of the coordinate bond between the SAM molecules and gold electrodes high-voltage SAMFETs are first fabricated and the impact of thermal annealing on device performance is also examined. SAMs are assembled via immersion at room temperature on a traditional dielectric platform (Figure 11b) previously used by our group for both thin film transistors [22] and SAMFETs [23]. After SAM assembly and cleaning to remove aggregates, substrates are annealed either before or after gold electrode deposition at 120 °C for 10 hour as seen in Figure 12a. Remarkably, Figure 12b shows a considerable shift in performance comparing devices that are not annealed, annealed before electrode deposition, and annealed after electrode deposition. Devices not annealed show no performance with the inability to act as a switch. Figure 12c shows that devices annealed before electrode deposition have some limited charge mobility of around  $10^{-5} \text{ cm}^2 \text{ V}^{-1} \text{ s}^{-1}$  while devices annealed after electrode deposition show two orders of magnitude increase in charge mobility to  $10^{-3} \text{ cm}^2 \text{ V}^{-1} \text{ s}^{-1}$ .

In terms of yield, roughly half of all devices annealed before electrode deposition function properly, while the yield for devices annealed after electrode deposition is near unity. Interestingly, this enhancement is accompanied by a shift in apparent threshold voltage ( $V_t$ ) as can be seen in Figure 12d. Devices annealed before or after electrode deposition exhibited an apparent threshold voltage of around -80 V and -65 V respectively. While  $V_t$  remains constant across tested channel lengths regardless of odd or even alkyl chain of SAMFET molecules, the impact of annealing before or after electrode deposition plays a clear role and elucidates a potential mechanism for the shown performance enhancement.

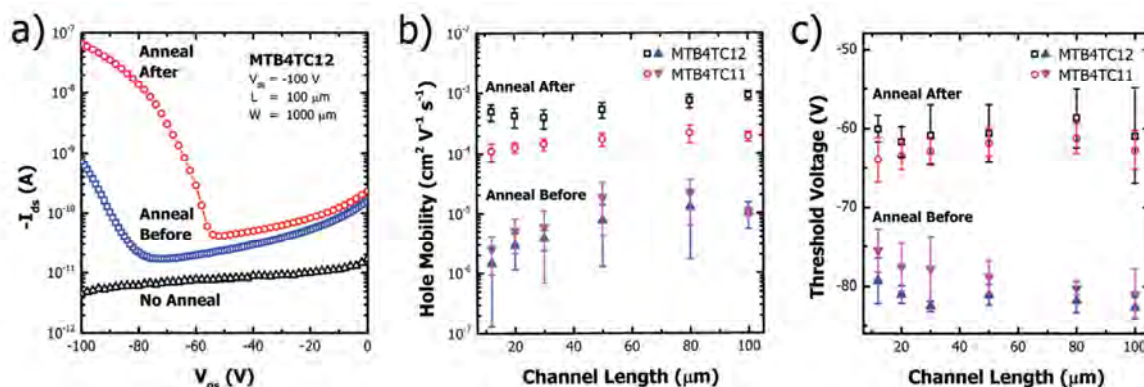


**Figure 12.** Anneal before indicates SAM annealing at 120 °C for 10 hours before electrode deposition and anneal after, indicates SAM annealing at 120 °C for 10 hours after electrode deposition; a) Characteristic transfer curve for high-voltage SAMFETs with MTB4TC12 semiconductor SAM with different annealing routes; Transistor performance parameters for b) hole mobility and c) threshold voltage based on SAM semiconductor and annealing route. Data are averaged of approximately 7 devices per channel length and are for transistors with a channel width of 1000  $\mu\text{m}$

$V_t$  is generally thought to be related to the surface density of deeply trapped charges in the channel and contact region of a transistor [24]. Deep traps, which are considered to be a few kT above the highest occupied molecular orbital, may occur due to structural defects and impurities [25]. It is likely that the deposition of gold on top of the SAM semiconductor resulted in the formation of such trap states through the creation of local structural disorder. The morphology of unannealed gold on top of the SAM (Figure 13a) shows morphology consistent with having a high density of trap sites due to the numerous small grains and subsequent grain boundaries. However, upon annealing at 120 °C (Figure 13b), these grains coarsen to form large interconnected grains. Evidence of this morphology change indicates that the gold atoms are able to reorganize to a more energetically favorable morphology to allow for better contact between electrode and SAM semiconductor resulting in reduced trap sites. This reduction in trap site density due to grain coarsening may also be a contributing factor for the mobility enhancement that occurs upon annealing post electrode deposition.

Another mechanism for enhanced mobility is most likely related to a reduced charge injection barrier at the Au-SAM interface. A threshold voltage shift accompanied by improved mobility due to changes between metal electrodes and semiconductor has been found earlier for both thin film organic transistors with SAM modified gold electrodes and monolayer  $\text{MoS}_2$  transistors with different metal electrodes [26-27]. The reduced charge injection barrier for devices fabricated in this manuscript is thought to be enabled by the intimate contact formed between the sulfur of the SAM semiconductor and the gold atoms. Thermal annealing after gold electrode deposition is needed to further strengthen the coordinate bond between SAM and electrode which requires a separation distance of less than 0.5 nm [28]. It is hypothesized that annealing post-electrode deposition provides enough thermal energy for reorganizing SAM molecules, gold atoms, or both to improve contact.

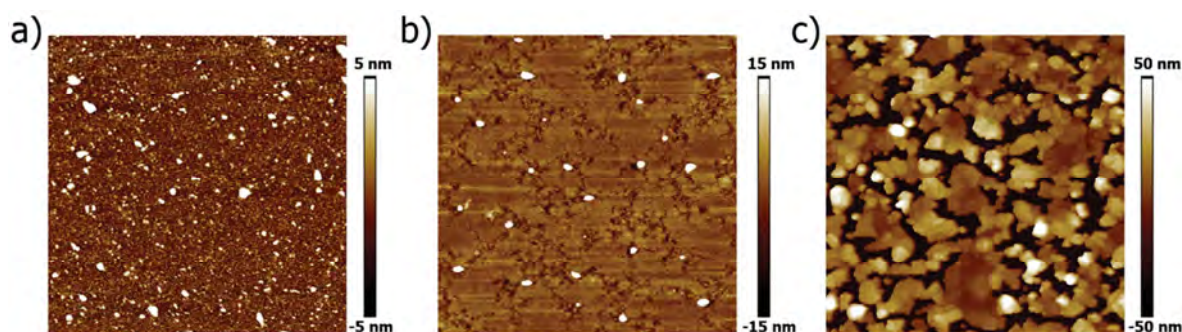


**Figure 13.** Representative morphology of Au on top of MTB4TC11 SAM assembled on  $\text{AlO}_x$  measured by tapping mode atomic force microscopy for a) no anneal, b) anneal after, and c) over annealed substrates.

However, it is known that if temperatures are elevated to around 300 °C, the mobile gold atoms will cause the sulfide to desorb from the surface [29]. It was found that over annealing to above 150 °C will result in gold dewetting from the SAM surface and forming isolated islands of gold (Figure 13c). Such a phenomenon is accompanied by a significant reduction in device performance.

In order to further enhance SAMFET performance, SAM immersion assembly temperature is optimized. Traditionally, for the assembly of SAMs, solvents with a dielectric constant ( $\epsilon_r$ ) between 3 and 5 are found to be optimal. It is believed that if the solvent  $\epsilon_r$  is below 3, SAMs tend to form micelles. If greater than 5, solvent will interact too strongly with the SAM to disrupt assembly at the substrate-solution interface [30-31]. In our study, dimethyl sulfoxide (DMSO) was found to provide the greatest solubility allowing for higher SAM solution concentration without forming aggregate. However, DMSO has a relatively high dielectric constant ( $\sim 46$ ), which may limit the dense assembly of SAM.

High-voltage SAMFET devices using the same device architecture shown in Figure 11b with varying SAM immersion assembly temperatures were fabricated and characterized. Morphology of SAMs assembled at room temperature and 120°C were found to be similar for both MTB4TC11 and MTB4TC12. SAMs assembled at room temperature had rms roughness values of 0.26 nm and 0.46 nm for MTB4TC11 and MTB4TC12, respectively while SAMs assembled at 120°C had rms roughness values of 0.33 nm and 0.43 nm, respectively. Representative morphologies characterized by tapping mode atomic force microscopy are shown in Figure 14a.

The static water contact angle for MTB4TC12 SAMFETs was found to increase slightly from  $71.4^\circ \pm 0.8^\circ$  to  $76.2^\circ \pm 0.9^\circ$ , respectively, when comparing assembled at room temperature versus 120 °C. This slightly increased contact angle may be indicative of increased SAM density. The relationship between SAM assembly temperature and density is further corroborated from X-ray photoelectron spectroscopy data which suggests an approximately 30% increase in SAM density between room temperature and 120°C assembly conditions. This improved SAM density results in an order of magnitude higher hole-mobility as shown in Figure 14b. This follows an expected trend of increasing mobility with respect to assembly temperature from room temperature to 120 °C while other parameters such as on/off current ratio, threshold voltage, and subthreshold swing remain relatively constant regardless of assembly temperature. Representative transfer and output curves of high voltage SAMFETs with MTB4TC11 are shown in Figure 14c and 14d.



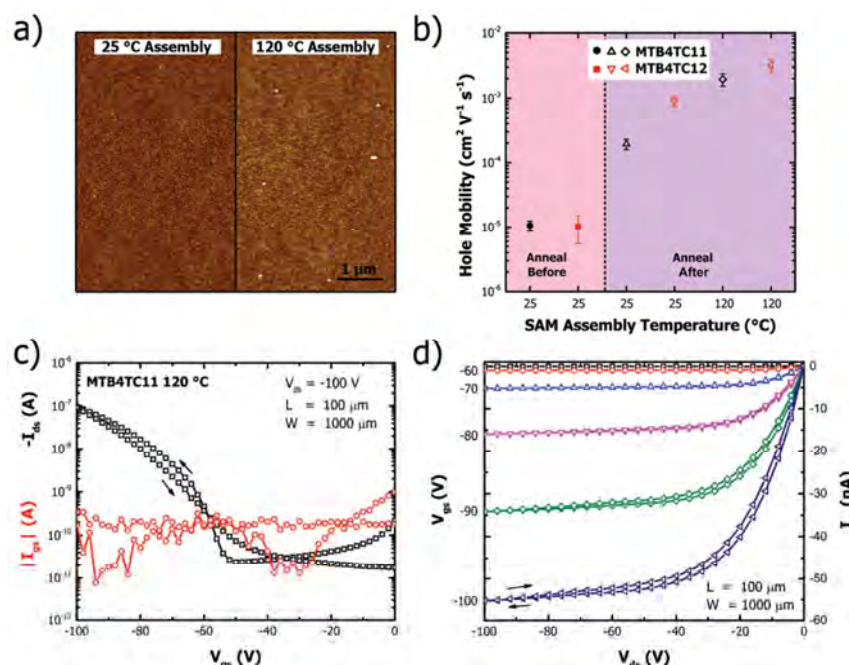


**Figure 14.** a) Representative morphology measured via AFM of MTB4TC11 SAM on AlO<sub>x</sub> assembled at 25 °C (left) and 120 °C (right) with a 5 nm height scale. b) Hole mobility of high-voltage SAMFETs with either MTB4TC11 or MTB4TC12 SAM semiconductor assembled at 25 °C or 120 °C. The first two left most data points indicate performance for devices annealed before electrode deposition while last four data points indicate performance for devices annealed after electrode deposition. Data is for transistors with channel width and length of 1000  $\mu$ m and 100  $\mu$ m respectively and is an average of at least 5 devices. c) Representative transfer and d) output characteristic transistor curves for a MTB4TC11 SAM assembled at 120 °C SAMFET and annealed after electrode deposition at 120 °C for 10 h with a channel width and length of 1000  $\mu$ m and 100  $\mu$ m respectively.

To obtain a better insight of the overall quality of SAMs assembled at 120 °C, the SAM/electrode interface, and the impact of annealing, SAMs of MTB4TC11 were characterized with near edge X-ray absorption fine structure (NEXAFS) spectroscopy. NEXAFS can provide chemical identification of specific bonds within SAMs and detailed information about molecular alignment [32]. Substrates with MTB4TC11 SAM were half covered with a 3 nm thick gold layer to allow for the characterization via NEXAFS of MTB4TC11 SAM with or without gold. After gold deposition, a subset of substrates were then annealed at 120 °C for 2 hour to allow the determination of the influence of both gold and annealing post gold deposition.

Carbon K-edge spectra, collected at an x-ray incident angle of 55°, from annealed/unannealed versions of MTB4TC11 and Au coated MTB4TC11 are presented in Figure 15a and 15b. The absorption near 285 eV, related to  $\pi^*$  C=C orbitals within the quaterthiophene groups, is present in all spectra taken from all variants of the MTB4TC11 SAM [33]. Moving to higher x-ray energies we observe a peak at 287 eV related to R\*/C-H  $\sigma^*$  molecular orbitals [34]. The orientation and ordering of molecular bonds can be assessed by changes in the x-ray absorption as the sample is rotated relative to the incident x-ray beam by  $\theta$ . Difference spectra (90°-20°), from annealed/unannealed versions of MTB4TC11 and Au coated MTB4TC11 are also shown in Figure 15a and 15b.

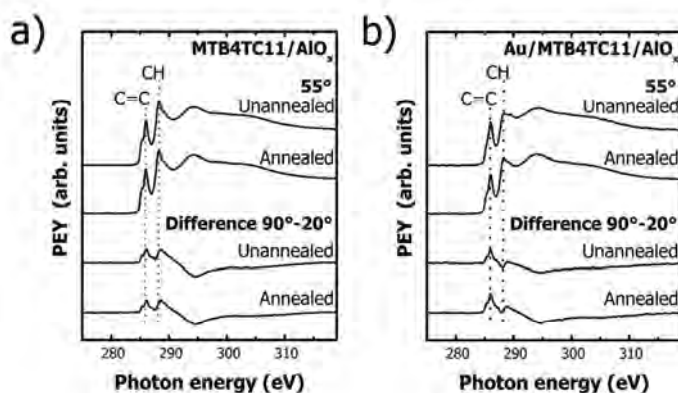


**Figure 15.** NEXAFS C K-edge spectra from unannealed and annealed samples of a) MTB4TC11 on  $\text{AlO}_x$  and b) Au coated MTB4TC11 on  $\text{AlO}_x$ . Each figure contains spectra collected at X-ray incidence angles of  $55^\circ$  (top traces) along with differences of spectra recorded at  $90^\circ$  and  $20^\circ$  (bottom traces).

In all cases, the NEXAFS spectra show a high degree of ordering (positive dichroism) of  $\pi^*$  C=C molecular orbitals. We have modeled the angle dependence of the  $\pi^*$  resonance to calculate the orientation of the thiophene units before and after gold deposition using standard procedures. Relative to the surface normal, the thiophene tilt angles for unannealed and annealed MTB4TC11 are  $29.5^\circ$  and  $30.5^\circ$  respectively. This apparent lack in change of tilt angle seems to indicate that annealing by itself may not result in significant molecular reorientation. However, upon depositing gold on top of the MTB4TC11 SAM the thiophene units became more upright. For the unannealed sample set, the thiophene tilt angle is determined to be  $26.3^\circ$ . For the sample set where gold was annealed after deposition on MTB4TC11 SAM, the thiophene tilt angle is determined to be  $24.4^\circ$ . The SAMs may become more upright when covered with gold due to the proposed coordinate bond between sulfur and gold. Additionally, the greater change in thiophene tilt angle between pristine SAM and SAM covered with gold ( $6^\circ$  and  $3^\circ$  for annealed and unannealed respectively) indicates annealing with gold facilitates an interaction between SAM and gold. A similar trend with the comparison molecule B4TC11 is also found which may indicate that the gold is not limited to interact with just the methyl sulfide functional group but may also interact with the sulfur present in the quaterthiophene semiconducting core. The molecular architecture can introduce some uncertainty in the angle determination (twist, torsion angles etc). These errors do not apply for systems which use the same molecules: MTB4TC11 or B4TC11 (before and after anneal, or before and after gold deposition). The error margin comparing within a given molecule set is less than 1 degree. Comparing between datasets we can assume a margin of 2.5 degree. We have some statistics because we use three different ratios within the dataset to calculate and we get standard deviations of about 0.2 degrees. The rest of the error includes experimental inaccuracies. Errors introduced by data analysis are largely eliminated because we use intensity ratios and not absolute values. So small inaccuracies induced by normalization cancel out. Overall, this NEXAFS dataset provides enough information to show that depositing gold on top of these SAMs results in the thiophenes orienting more upright which is then slightly increased with the addition of an annealing step.

In order to understand the influence of the methylthio functional group a comparison molecule ((11-(5'''-butyl-[2,2':5',2'':5'',2'''-quaterthiophen]-5-yl)undecyl)phosphonic acid, B4TC11) was used. Comparing performance data of B4TC11 to MTB4TC11 allows us to further clarify the advantages and disadvantages of the two functional groups. SAMs of B4TC11, MTB4TC11, and MTB4TC12 were assembled on  $\text{HfO}_2$  via the heated assembly procedure at  $120^\circ\text{C}$  as described earlier for  $\text{AlO}_x$ . In order to verify the quality of SAM, static water contact angle for MTB4TC12 was determined at  $77.1^\circ \pm 0.3^\circ$  which is comparable to



the data previously reported on  $\text{AlO}_x$ . Additionally, the contact angle of B4TC11 was found to be at  $87.3^\circ \pm 0.4^\circ$  which is comparable to literature data [35]. Furthermore, the rms roughness determined by AFM of MTB4TC12 was found to be 0.32 nm further indicating the presence of a quality monolayer on the  $\text{HfO}_2$  dielectric platform that is comparable to that of our  $\text{AlO}_x$  platform.

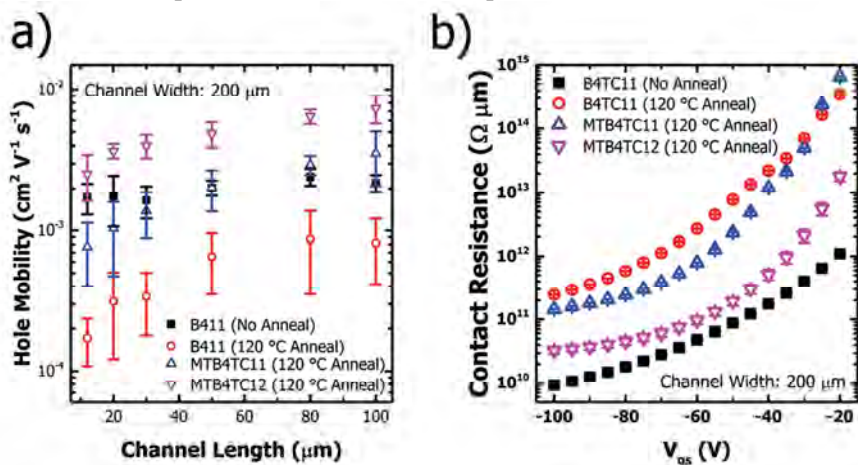


**Figure 16.** a) Hole mobility with respect to channel length for high voltage SAMFETs with a  $\text{HfO}_2/300\text{nm SiO}_2/\text{Si}$  dielectric/gate stack and SAM semiconductors B4TC11, MTB4TC11, and MTB4TC12. Performance is indicated if devices are not annealed or are annealed at 120 °C for 10 h after 50 nm Au electrode deposition. b) Contact resistance with respect to gate-source voltage of high-voltage SAMFETs with  $\text{HfO}_2$  dielectric stack.

Performance data for the series of fabricated devices can be seen in Figure 16a. Surprisingly, it was found that our control molecule B4TC11 yielded a hole mobility of  $0.00213 \text{ cm}^2 \text{V}^{-1} \text{s}^{-1}$  for pristine unannealed devices. However, upon annealing the devices at 120 °C for 10 hour after electrode deposition the hole mobility was reduced by nearly an order of magnitude. A similar trend was also seen for an even lower temperature anneal of 80°C. This reduction in hole mobility seems to indicate that devices with only a butyl functional head group have limited thermal stability and that annealing results in damage at the SAM/electrode interface. This damage may be caused by diffusion of gold atoms into the SAM semiconductor core resulting in disruption of local SAM molecular order that is integral for charge carrier transport. Comparatively, our MTB4TC11 and MTB4TC12 devices initially exhibit little to no performance without annealing. However, upon annealing after electrode deposition the hole mobility for MTB4TC11 and MTB4TC12 increases to  $0.00356 \text{ cm}^2 \text{V}^{-1} \text{s}^{-1}$  and  $0.00737 \text{ cm}^2 \text{V}^{-1} \text{s}^{-1}$  respectively. Additionally, since MTB4TC11 has better mobility compared to unannealed B4TC11 and about one order of magnitude higher hole mobility compared to annealed B4TC11 devices, the influence of the methylthio functional group seems to help enhance device mobility as well as increase thermal stability by protecting the semiconducting core from being disrupted by the gold electrodes.

In order to further understand the influence of the SAM functional head group, contact resistance was determined using a modified transmission line method [36]. Contact resistance with respect to gate-source voltage is shown in Figure 6b. It was found that even though MTB4TC12 exhibited the best device performance, the unannealed B4TC11 devices had the low contact resistance. This is reasonable given that it has the shortest functional head group of the systems tested. However, as expected, upon annealing after electrode deposition the contact resistance of B4TC11 becomes the highest among tested architectures. This further verifies that the effect of the methylthio functional group seems to help increase thermal stability by protecting the semiconducting core from being disrupted by the gold electrodes upon heating.

While high-voltage devices in this paper serve to elucidate the importance of device processing and design for SAMFETs, real-world applications rely on having low operating voltage devices. Optimized processing conditions have been used to fabricate low-voltage MTB4TC12 SAMFETs on a thin  $\text{HfO}_2$  dielectric as seen in the insert of Figure 17a.  $\text{HfO}_2$  is a proven high- $k$  dielectric that has previously been used for low-voltage thin film organic transistors [37]. Fabricated metal-insulator-metal junctions of  $\text{HfO}_2$  show a low current density of  $2.1 \times 10^{-8} \text{ A cm}^{-2}$  at -3 V and capacitance of  $565 \text{ nF cm}^{-2}$  at a frequency of 1 kHz. However, it is important to take into account the additional capacitance provided by the dodecyl alkyl chain of the MTB4TC12 SAM used which is estimated to lower the total capacitance to  $408 \text{ nF cm}^{-2}$ . Low voltage SAMFETs exhibited excellent charge carrier mobility with the best hole-mobility reaching  $0.015 \text{ cm}^2 \text{ V}^{-1} \text{ s}^{-1}$  for devices with a channel width and length of  $200 \mu\text{m}$  and  $100 \mu\text{m}$  respectively.

Figure 17a shows that mobility increases with decreasing channel width/length ratio indicating that total contact area is critical to device performance. A similar trend is also seen for high-voltage devices and is indicative of performance being limited by resistance within the transistor circuit. As shown in Figure 17b and comparable to high voltage SAMFETs, on/off current ratios of  $10^3$  are found which stems from the reduced off current present in low voltage devices. Additionally, devices are found to have an excellent differential between drain-source current and gate-source leakage current at around  $10^2$ . This exemplifies the high quality nature of our sol-gel  $\text{HfO}_2$  hybrid dielectric as it is currently the highest reported value for low voltage SAMFET devices. Representative transfer and output characteristics for a device with channel width and length of  $200 \mu\text{m}$  and  $100 \mu\text{m}$  respectively is shown in Figure 17c and 17d.

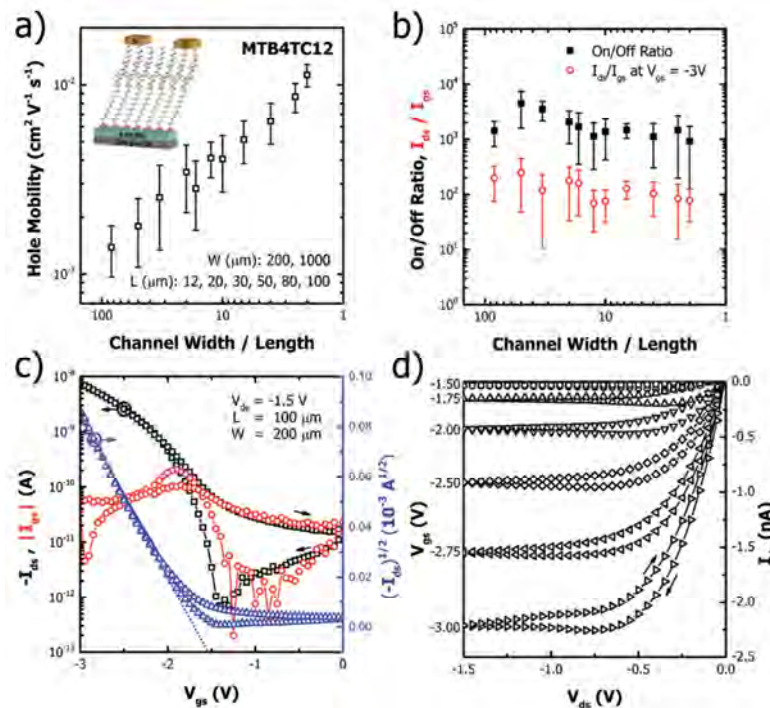


**Figure 17.** a) Hole mobility with respect to ratio of channel width/length for low voltage SAMFET with MTB4TC12 SAM semiconductor with insert showing device architecture; Device assembled under best conditions with SAM assembly at  $120^\circ \text{C}$  and device annealed at  $120^\circ \text{C}$  for 10 hours after gold electrode deposition; b) Transistor performance parameters indicating on/off current ratio, and difference between drain-source current and gate-source leakage current at -3 V; Representative transfer (c) and output (d) characteristic transistor curves for a device with a channel width and length of  $200 \mu\text{m}$  and  $100 \mu\text{m}$  operated at  $V_{ds}$  of -1.5 V.

#### 4. Conclusion

In summary, high performance low operating voltage SAMFETs have been fabricated through the rational design of a functional SAM head group and processing optimization. The methylthiobutyl terminal group of the quaterthiophene based SAM semiconductors has enabled efficient electrical contact to Au electrodes while maintaining SAMFET thermal stability. Annealing has been shown to further enhance the coordinate bond between SAM and electrode to enable over two orders of magnitude increase in charge carrier mobility. Additionally, through the use of heated immersion assembly, SAM density has been increased by approximately 30% resulting in another order of magnitude higher charge carrier mobility. Low voltage SAMFETs utilizing hybrid HfO<sub>2</sub> sol-gel dielectric were then assembled under optimized processing conditions to achieve a peak hole-mobility of 0.015 cm<sup>2</sup> V<sup>-1</sup> s<sup>-1</sup>. These results show the importance of terminal group and processing for SAMFETs and should be generally applicable to other SAM semiconductor systems.

#### 5. References

- [1] P. Heremans, G. H. Gelinck, R. Muller, K.-J. Baeg, D.-Y. Kim, Y.-Y. Noh, *Chem. Mater.* **2011**, *23*, 341-358.
- [2] S. M. Sze, *Physics of Semiconductor Devices* **1981**, 2<sup>nd</sup> Edition, 496-507.
- [3] C. Kim, J.-M. Song, J.-S. Lee, M. J. Lee, *Nanotechnology* **2014**, *25*, 014016.
- [4] T. Sekitani, T. Yokota, U. Zschieschang, H. Klauk, S. Bauer, K. Takeuchi, M. Takamiya, T. Sakurai, T. Someya, *Science* **2009**, *326*, 1516-1519.
- [5] T.-W. Kim, Y. Gao, O. Acton, H.-L. Yip, H. Ma, H. Chen, A. K.-Y. Jen, *Appl. Phys. Lett.* **2010**, *97*, 023310.
- [6] A. Rani, J.-M. Song, M. J. Lee, J.-S. Lee, *Appl. Phys. Lett.* **2012**, *101*, 233308.
- [7] S.-T. Han, Y. Zhou, Q. D. Yang, L. Zhou, L.-B. Huang, Y. Yan, C.-S. Lee, V. A. L. Roy, *Nano Lett.* **2014**, *8*, 1923-1931.
- [8] MoS<sub>2</sub> memory window increased with layer decrease
- [9] M. Halik, A. Hirsch, *Adv. Mater.* **2011**, *23*, 2689.
- [10] E. C. P. Smits, S. G. J. Mathijssen, P. A. van Hal, S. Setayesh, T. C. T. Geuns, K. A. H. A. Mutsaers, E. Cantatore, H. J. Wondergem, O. Werzer, R. Resel, M. Kemerink, S. Kirchmeyer, A. M. Muzafarov, S. A. Ponomarenko, B. de Boer, P. W. M. Blom, D. M. de Leeuw, *Nature* **2008**, *455*, 956.
- [11] T. Schmaltz, A. Y. Amin, A. Khassanov, T. Meyer-Friedrichsen, H. G. Steinruck, A. Magerl, J. J. Segura, K. Voitchovsky, F. Stellacci, M. Halik, *Adv. Mater.* **2013**, *25*, 4511.
- [12] A. Ringk, X. Li, F. Gholamrezaie, E. C. P. Smits, A. Neuhold, A. Moser, C. Van der Marel, G. H. Gelinck, R. Resel, D. M. de Leeuw, P. Strohmriegel, *Adv. Funct. Mater.* **2013**, *23*, 2016.
- [13] A. V. S. Parry, K. Lu, D. J. Tate, B. Urasinska-Wojcik, D. Caras-Quintero, L. A. Majewski, M. L. Turner, *Adv. Funct. Mater.* **2014**, *24*, 6677.
- [14] F. Dinelli, M. Murgia, P. Levy, M. Cavallini, F. Biscarini, D. M. de Leeuw, *Phys. Rev. Lett.* **2004**, *92*, 116802.
- [15] A. Shehu, S. D. Quiroga, P. D'Angelo, C. Albonetti, F. Borgatti, M. Murgia, A. Scorzoni, P. Stoliar, F. Biscarini, *Phys. Rev. Lett.* **2010**, *104*, 246602.
- [16] J. Zhu, M. Chen, H. Qu, Z. Luo, S. Wu, H. A. Colorado, S. Wei, Z. Guo, *Energy Environ. Sci.* **2013**, *6*, 194.
- [17] J. P. Folkers, C. B. Gorman, P. E. Laibinis, S. Buchholz, G. M. Whitesides, R. G. Nuzzo, *Langmuir* **1995**, *11*, 813.
- [18] F. Garnier, R. Hajlaoui, A. El Kassmi, G. Horowitz, L. Laigre, W. Porzio, M. Armanini, F. Provasoli, *Chem. Mater.* **1998**, *10*, 3334.

- [19] S. A. Ponomarenko, O. V. Borshchev, T. Meyer-Friedrichsen, A. P. Pleshkova, S. Setayesh, E. C. P. Smits, S. G. J. Mathijssen, D. M. de Leeuw, S. Kirchmeyer, A. M. Muzafarov, *Organometallics* **2010**, *29*, 4213.
- [20] J. Noh, H. S. Kato, M. Kawai, M. Hara, *J. Phys. Chem. B* **2002**, *106*, 13268.
- [21] Y. S. Park, A. C. Whalley, M. Kamenetska, M. L. Steigerwald, M. S. Hybertsen, C. Nuckolls, L. Venkataraman, *J. Am. Chem. Soc.* **2007**, *129*, 15768.
- [22] D. O. Hutchins, O. Acton, T. Weidner, N. Cernetic, J. E. Baio, D. G. Castner, H. Ma, A. K.-Y. Jen, *Appl. Surf. Sci.* **2012**, *261*, 908.
- [23] D. O. Hutchins, O. Acton, T. Weidner, N. Cernetic, J. E. Baio, G. Ting, D. G. Castner, H. Ma, A. K. Y. Jen, *Org. Electron.* **2012**, *13*, 464.
- [24] Q.-J. Sun, Z. Xu, S.-L. Zhao, F.-J. Zhang, L.-Y. Gao, Y.-S. Wang, *Synth. Met.* **2010**, *160*, 2239.
- [25] S. D. Wang, T. Minari, T. Miyadera, Y. Aoyagi, K. Tsukagoshi, *Appl. Phys. Lett.* **2008**, *92*, 063305.
- [26] M. Kitamura, Y. Kuzumoto, S. Aomori, M. Kamura, J. H. Na, Y. Arakawa, *Appl. Phys. Lett.* **2009**, *94*.
- [27] S. Das, H.-Y. Chen, A. V. Penumatcha, J. Appenzeller, *Nano Lett.* **2012**, *13*, 100.
- [28] M. Tachibana, K. Yoshizawa, A. Ogawa, H. Fujimoto, R. Hoffmann, *J. Phys. Chem. B* **2002**, *106*, 12727.
- [29] D. O. Bellisario, A. D. Jewell, H. L. Tierney, A. E. Baber, E. C. H. Sykes, *J. Phys. Chem. C* **2010**, *114*, 14583.
- [30] H.-Y. Nie, M. J. Walzak, N. S. McIntyre, *J. Phys. Chem. B* **2006**, *110*, 21101.
- [31] Y. Ito, A. A. Virkar, S. Mannsfeld, J. H. Oh, M. Toney, J. Locklin, Z. Bao, *J. Am. Chem. Soc.* **2009**, *131*, 9396.
- [32] J. Stöhr, NEXAFS Spectroscopy, Vol. **25**, Springer-Verlag, Berlin 1992.
- [33] H.-J. Himmel, A. Terfort, C. J. Wöll, *J. Am. Chem. Soc.* **1998**, *120*, 12069.
- [34] D. A., Outka, J. Stöhr, J. P. Rabe, J. D. J. Swalen, *J. Chem. Phys.* **1988**, *88*, 4076.
- [35] M. Novak, A. Ebel, T. Meyer-Friedrichsen, A. Jedaa, B. F. Vieweg, G. Yang, K. Voitchovsky, F. Stellacci, E. Spieker, A. Hirsch, M. Halik, *Nano Lett.* **2011**, *11*, 156.
- [36] Y. Xu, R. Gwoziecki, I. Chartier, R. Coppard, F. Balestra, G. Ghibaudo, *Appl. Phys. Lett.* **2010**, *97*, 063302.
- [37] O. Acton, M. Dubey, T. Weidner, K. M. O'Malley, T.-W. Kim, G. G. Ting, D. Hutchins, J. E. Baio, T. C. Lovejoy, A. H. Gage, D. G. Castner, H. Ma, A. K. Y. Jen, *Adv. Funct. Mater.* **2011**, *21*, 1476.

## 1. Introduction

The desirable properties and increased availability of single- and few-layer graphene have motivated interest in interfacing functional molecules and materials to its high surface area basal plane. The surface of pristine graphene lacks chemical functionality to allow for covalent modification without interrupting its continuous  $\pi$ -orbital system. In contrast, noncovalent functionalization does not suffer from these drawbacks and offers a means to tune graphene properties and incorporate molecular recognition or other active elements [1,2]. For example, an adsorbed molecular lattice is able to impose a super-period to graphene atomic lattice which is considered as a new mean to finely tune its band and sub-band structure in view of innovative 2D semiconductor junctions [3]. On the other hand, the principles of supramolecular chemistry offer promising routes to design specific molecular assemblies fulfilling the needs of functional surfaces by noncovalent functionalization [4-5]. A series of synthesis protocols have already been tested employing, e.g. van der Waals force [6]. Recently, we proposed a strategy to form “on-demand” noncovalent self-assemblies with predetermined 2D topologies on highly oriented pyrolytic graphite (HOPG) at the liquid/solid interface at room temperature [7-8]. This approach is based on a new functional group for surface specific self-assembly at surfaces (‘molecular clip’)[7]. Then, we are able to pattern the surface with either flat or functionalized 3D molecules (Janus tectons) leading to nanoporous networks [7-8]. In the present project, we proposed to exploit this approach to achieve 'host-guest' systems based on (i) a 2D nanoporous organic matrix capable of capturing the inorganic magnetic nanocrystals or (ii) the Janus tecton concept as ligands.

Here we demonstrated that it is possible (1) to extend to graphene the approaches we developed for the steered supramolecular self-assembly, and (2) to synthesize building-blocks bearing ligands in view of catching nanoparticles.

## 2. Results and Discussion

### 2.1. Supramolecular Self-assembly on Graphene

(1) First, we confirmed that the concept we developed for steered self-assembly on HOPG works on graphene. In Figure 18 bellows are reported, for comparison, the STM images on HOPG and a CVD monolayer graphene on polycrystalline Cu of self-assembled honeycomb nanoporous structure. The structure is clearly preserved upon changing HOPG for graphene. This very preliminary result indicates that our strategy works on graphene leading to similar self-assembly.

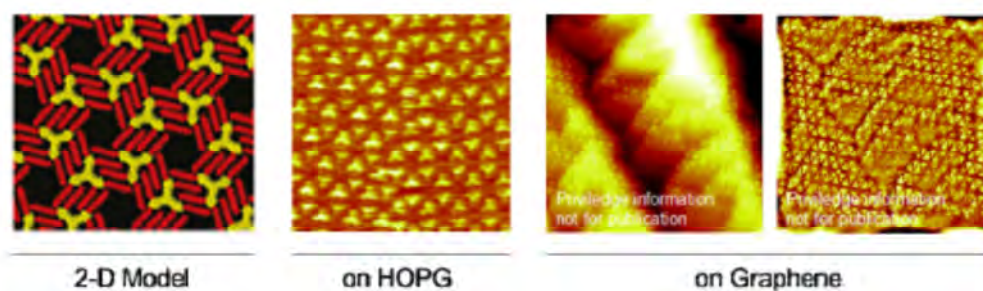


**Figure 18.** STM images on HOPG and and a CVD monolayer graphene on polycrystalline Cu of self-assembled honeycomb nanoporous structure.

(2) A general strategy for simultaneously generating surface-based supramolecular architectures on flat  $sp^2$ -hybridized carbon supports and independently exposing on demand off-plane functionality with



controlled lateral order is highly desirable in view of the noncovalent functionalization of graphene. Here, for the first time, we address this issue by providing a versatile molecular platform based on a library of new 3D Janus tectons able to form surface-confined supramolecular adlayers in which it is possible to simultaneously (i) steer the 2D self-assembly on flat  $sp^2$ -carbon based substrates with controlled lateral order to form periodic patterns and (ii) tailor the external interface above the substrate by exposing a wide variety of small terminal chemical groups and functional moieties [10]. The results are reported in Figure 19.

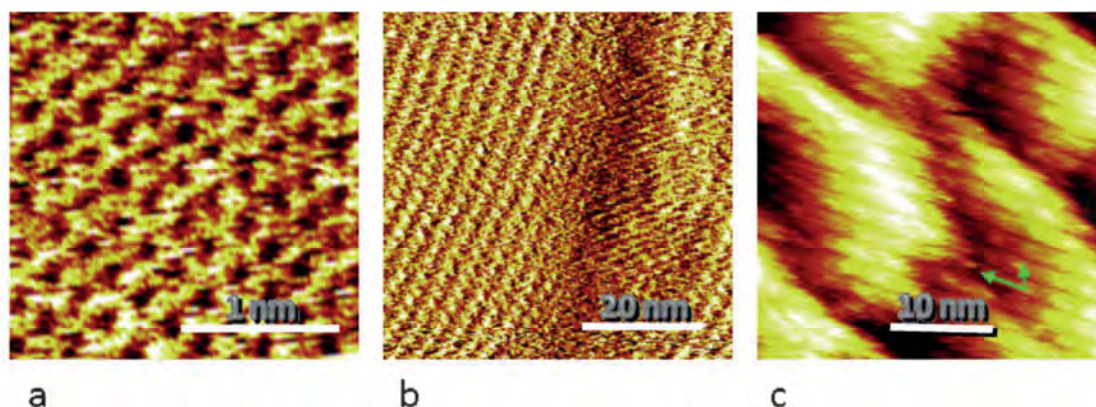


**Figure 19.** Self-assembly on graphene. Drift-corrected STM images obtained: (a) in air on a monolayer graphene substrate grown by chemical vapor deposition on a polycrystalline copper foil showing the alveolar graphene atomic structure (2.2x2.2 nm, setpoint  $I_T=110$  pA, sample bias  $V_B=-350$  mV), and (b,c) at the interface between this substrate and a  $10^{-4}$ M solution of Janus tectons in phenyloctane (b: 58x58 nm, set point  $I_T=20$  pA, sample bias  $V_B=-950$  mV; c: 34x34 nm,  $I_T=13$  pA,  $V_B=-950$  mV). Images (a) and (b) were acquired in the current (i.e. so-called constant height) mode, whereas image (c) was acquired in the height (i.e. constant current) mode to show the substrate roughness. A unit cell corresponding to the lattice formed on HOPG ( $a=3.84$  nm,  $b=2.08$  nm, and  $\alpha=648$ ) is highlighted in c) (green arrows).

First, the atomically resolved alveolar structure of graphene was observed by STM, without application of the Janus tecton solution Figure 19a. Then, images were acquired, at the interface between the graphene and the Janus tecton solution, Figure 19b,c. Although the imaging conditions are less stable than for HOPG, the molecular network is clearly observed through the conjugated function of the Janus tectons, with lattice parameters compatible with those obtained on graphite. Strikingly, the monolayer domains extend over rough areas and protrusions on the substrate imposed by the polycrystalline copper carrier material (as shown by Figure 19b, which was acquired over a particularly rough surface area). This shows, first, that the top-most atomic layer is able to efficiently drive the self-assembly and, second, that the graphene foil provides a long-range crystalline structural coherence that extends far beyond the carrier material defects, thus permitting well-ordered self-assembly into rather large single domains. The stability of the monolayer under ambient conditions was assessed to be similar to as on HOPG.

The reported strategy is expected to be applicable generally for generating self-assembled Janus tectons exhibiting *on demand* functionalization applications in various fields such as catalysis, electronics, photonics, biology etc.

To conclude, the successful self-assembly on graphene of periodic structures is expected to strongly influence the resulting band structure and to allow the control of the electronic properties of graphene. These results are important in view of fabrication of graphene based transistors. Moreover, the long range lateral order achieved by self-assembly on graphene provides a rational and reproducible surface functionalization, a necessary requirement. Finally, the possibility to transfer the graphene monolayer onto various substrates, considerably expands the domains of application of our noncovalent functionalization strategy.

## 2.2. Synthesis of Building Blocks bearing Ligands

(a) In order to functionalize the cavities of the nanoporous networks, first the following building-block bearing a ligand with a terminal acid group was synthesized. The self-assembly of the tectons 2CA was investigated by STM at the interface between HOPG and a phenyloctane solution, at room temperature. The typical STM images are reported in Figure 20.

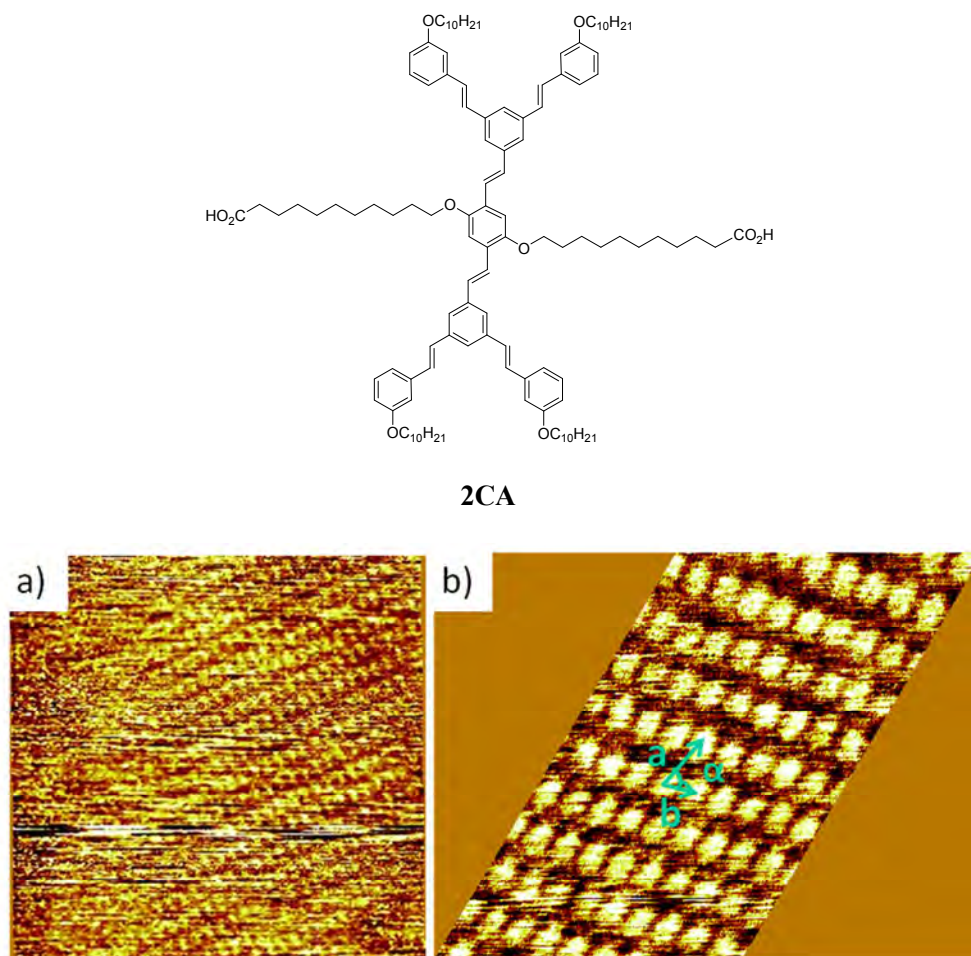
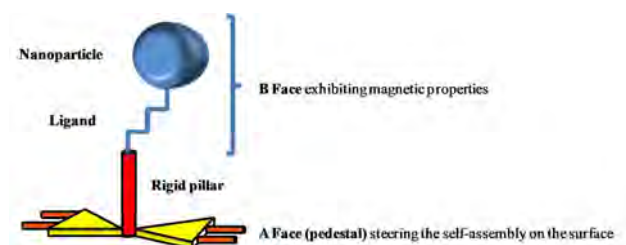


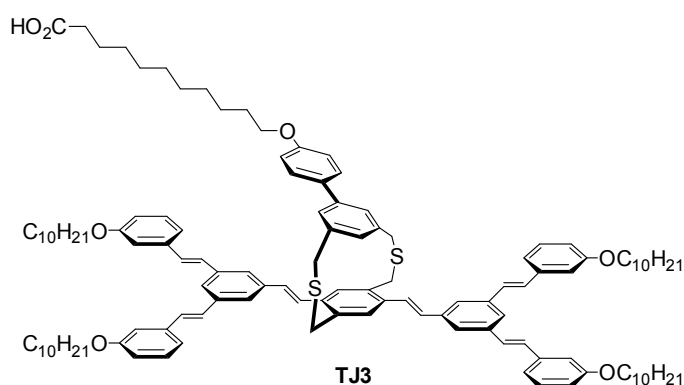
**Figure 20.** STM images of the tecton 2CA self-assembled on HOPG. a) ( $V_B = -965$  mV,  $I_T = 17$  pA,  $90 \times 90$  nm<sup>2</sup>), b) ( $V_B = -877$  mV,  $I_T = 17$  pA,  $30 \times 30$  nm<sup>2</sup>).

(b) In order to extend the concept of Janus tecton to catch magnetic nanoparticles, here we synthesize and adsorb on HOPG and graphene building blocks bearing a ligand to the upper deck of the pillar in order to promote ligand exchange.



*Janus 3D tecton exhibiting magnetic properties*

To achieve this objective, the following Janus tecton bearing a ligand with a terminal acid group was synthesized.



The self-assembly of this tectons was investigated by STM at the interface between HOPG and a phenyloctane solution, at room temperature. Figure u shows a typical STM image deposited on graphite and reveals that this 3D tecton forms a well-ordered adlayer on HOPG surface. The estimated unit cell dimensions are  $a=2.1\text{nm}$ ,  $b=3.9\text{nm}$  and  $\alpha=70^\circ$ . These values are in accordance, within experimental errors, with those obtained previously for other Janus tectons.

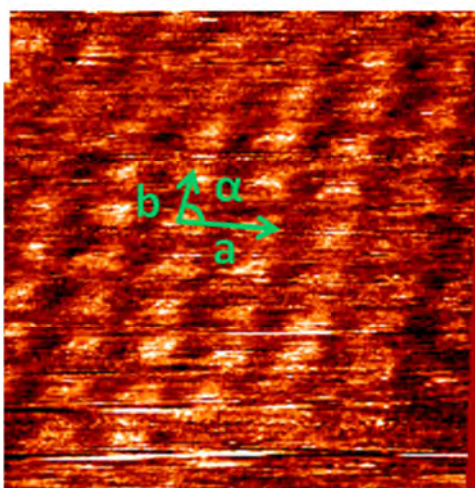


**Figure 21.** (a) STM image of Janus tecton TJ3,  $c = 5.10^{-5}\text{ M}$  ( $V_B = -688\text{ mV}$ ,  $I_T = 20\text{ pA}$ ,  $28 \times 28\text{ nm}^2$ ),  $a = 3,9\text{ nm}$ ,  $b = 2,1\text{ nm}$  et  $\alpha = 70^\circ$ .



### 2.3. Adsorption of Nanoparticles

As models we used platinum (Pt) nanoparticles capped with octylamine ( $C_8NH_2$ ), synthesized in the Christophe Petit's group at UPMC. They are mostly spherical and characterized by a mean diameter of around 2 nm. The attempts of characterization of the adsorbed nanoparticles by STM were unsuccessful. To avoid this drawback, current works deals with the characterization by scanning electron microscopy. Preliminary results (Figure 22) indicate that it's possible to catch the nanoparticles in the nanoporous network resulting of the self-assembly of molecule 2CA. Further investigations are in progress.

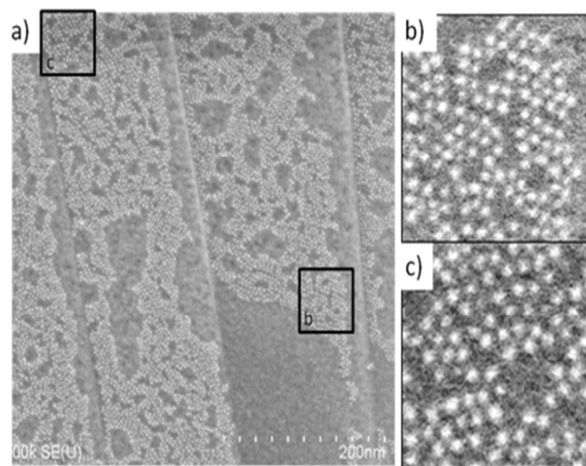


**Figure 22:** Scanning electron microscopy. Image of nanoparticles trapped in the nanoporous network resulting of the self-assembly of molecule 2CA

### 4. Conclusions

First, we demonstrated that we are able to self-assemble tectons able to form nanoporous networks on graphene. Moreover, the successful self-assembly on graphene of periodic structures is expected to strongly influence the resulting band structure and to allow the control of the electronic properties of graphene. These results are important in view of fabrication of graphene based transistors. Second, we are able to synthesize tectons (planar or 3D) bearing ligands in view of catching nanoparticles in the cavities of the nanoporous networks. Finally, if STM is not an adequate technique for the observation of the nanoparticles, preliminary results have been obtained by scanning electron microscopy

### 5. References

- [1] V. Georgakila, M. Otyepka, A. B. Bourlinos, V. Chandra, N. Kim, K. C. Kemp, P. Hobza, R. Zboril, K. S. Kim, *Chem. Rev.* **2012**, *112*, 6156-6214.
- [2] J. A. Mann, W. R. Dichtel, *J. Phys. Chem. Lett.* **2013**, *4*, 2649–2657.
- [3] P. Järvinen, S. K. Hämäläinen, K. Banerjee, P. Häkkinen, M. Ijäs, A. Harju, P. Liljeroth, *Nano Lett.* **2013**, *13*, 3199–3204.
- [4] J. V. Barth, G. Costantini, K. Kern, *Nature* **2005**, *437*, 671–679.
- [5] J. V. Barth, *Annu. Rev. Phys. Chem.* **2007**, *58*, 375–407.
- [6] J. A. A. W. Elemans, S. Lei, De Feyter *Angew. Chem., Int. Ed.* **2009**, *48*, 7298–7332.
- [7] D. Bleger, D. Kreher, F. Mathevet, A. J. Attias, G. Schull, A. Huard, L. Douillard, C. Fiorini-Debuischert, F. Charra, *Angew. Chem., Int. Ed.*, **2007**, *46*, 7404–7407.



- (4) K.-S. Lee, “Organic-Inorganic Hybrid Materials with Optoelectronic and Magnetic Functions”, 2<sup>nd</sup> Technical Meeting on Novel Nanomagnetic and Multifunctional Materials, James Clark School of Engineering, University of Maryland, Marland, USA, June 16-17 2014.
- (5) P. Du, M. Jaouen, Z. Han, V. Bouchiat, D. Kreher, F. Mathevet, C. Fiorini-Debuisschert, F. Charr, A.-J. Attias, “Surface-Confined Self-Assembled Janus Tectons: a Versatile Platform towards the Noncovalent Functionalization of Graphene”, 2<sup>nd</sup> Technical Meeting on Novel Nanomagnetic and Multifunctional Materials, James Clark School of Engineering, University of Maryland, Marland, USA, June 16-17 2014.
- (6) Y.S. Han, J.-H. Park, S.-H. Kim, S.-O. Kim, K.-E. Lee, K.-S. Lee, “Synthesis and Properties of Coupling Graphene Sheets with Magnetic Nanoparticles”, 2015 SPIE Photonics West, Moscone Center, San Francisco, Feb. 7-12, 2015.
- (7) S.-H. Kim, J.-H. Park, Y.-S. Han, S.-O. Kim, K. E. Lee, K.-S. Lee, “Graphene Sheets with Non-Covalently Coupled Magnetic Nanoparticles”, 45<sup>th</sup> IUPAC World Chemistry Congress, Bexco, Busan, Korea, August 9-14, 2015.